Interactions between depositional regime and climate proxies in the northern South China Sea since the Last Glacial Maximum

Xuesong Wang [1,8], Yi Zhong [2*], Peter D. Clift [3], Yingci Feng [4], David J. Wilson [5], Stefanie Kaboth-Bahr [6], André Bahr [7], Xun Gong [1,8], Debo Zhao [9], Zhong Chen [4], Yanan Zhang [2], Yuhang Tian [4], Yuxing Liu [2], Xiaoyu Liu [2], Jiabo Liu [11], Wenyue Xia [2], Huihui Yang [2,10], Wei Cao [2], Qingsong Liu [2,12*]

[1]Institute for Advanced Marine Research, China University of Geosciences, Guangzhou, China

[2]Centre for Marine Magnetism (CM[2]), Department of Ocean Science and Engineering, Southern University of Science and Technology, Shenzhen 518055, PR China

[3]Department of Geology and Geophysics, Louisiana State University, Baton Rough, LA, 70803, USA

[4]Key Laboratory of Ocean and Marginal Sea Geology, South China Sea Institute of Oceanology, Innovation Academy of South China Sea Ecology and Environmental Engineering, Chinese Academy of Sciences, Guangzhou 511458, China

[5]Department of Earth Sciences, University College London, London, UK

[6]Institute of Geosciences, University of Potsdam, Potsdam-Golm, Germany

[7]Institute of Earth Sciences, Heidelberg University, Im Neuenheimer Feld 234-236, 69120, Heidelberg, Germany

[8]State Key laboratory of Biogeology and Environmental Geology, Hubei Key

This article has been accepted for publication and undergone full peer review but has not been through the copyediting, typesetting, pagination and proofreading process, which may lead to differences between this version and the Version of Record. Please cite this article as doi: 10.1029/2022PA004591.

Laboratory of Marine Geological Resources, University of Geosciences, Wuhan 430074, China

[9]Key Laboratory of Marine Geology and Environment, Institute of Oceanology, Chinese Academy of Science, Qingdao

[10]Scholl of Environment, Harbin Institute of Technology, Harbin, China

[11]Paleomagnetism and Planetary Magnetism Laboratory, School of Geophysics and Geomatics, China University of Geosciences, Wuhan, Hubei 430074, China

[12]Shanghai Sheshan National Geophysical Observatory, Shanghai, 201602, China

*Corresponding author: Yi Zhong (zhongy@sustech.edu.cn), Qingsong Liu (qsliu@sustech.edu.cn)

Key Points:

- Sedimentary records from shallow and deep-water sites have differing sensitivities to changes in ocean currents and the East Asian monsoon.
- Clay mineralogy in shallow sites reflects sea-level change, while deep-water records respond to incursion of the Kuroshio Current.
- Magnetic grain-size indicates stronger deep currents during Heinrich Stadial 1, associated with the North Pacific Intermediate Water.

Abstract

Sedimentary deposits from the northern South China Sea (SCS) can provide important constraints on past changes in ocean currents and the East Asian summer monsoon in this region. However, the interpretation of such records spanning the last deglaciation is complicated because sea-level change may also have influenced the depositional processes and patterns. Here, we present new records of grain size, clay mineralogy, and magnetic mineralogy spanning the past 24 kyr from both shallow- and deep-water sediment cores in the northern SCS. Our multi-proxy comparison among multiple cores helps constrain the influence of sea-level change, providing confidence in interpreting the regional climate-forced signals. After accounting for the influence of sea-level change, we find that these multi-proxy records reflect a combination of changes in (i) the strength of the North Pacific Intermediate Water inflow, (ii) the East Asian summer monsoon strength, and (iii) the Kuroshio Current extent. Overall, this study provides new insights into the roles of varying terrestrial weathering and oceanographic processes in controlling the depositional record on the northern SCS margin in response to climate and sea-level fluctuations.

Plain Language Summary

Sediments in the South China Sea (SCS) provide important records of past changes in the ocean circulation and atmospheric patterns in the Pacific Ocean. However, the interpretation of sedimentary archives from this region in terms of changes in the ocean currents or the climate-driven sediment supply can be challenging because of the potential influence of global sea-level fluctuations. In order to better constrain these multiple controls on the sedimentary regime of the northern SCS, we present new mineralogical records from sediment cores collected from both shallow- and deep-water sites. After assessing the effects of sea-level change, we find that the clay mineral assemblage in shallow sites from the northern SCS can generally be used to reconstruct the evolution of the East Asian summer monsoon. In deep-water sites, the clay mineralogy instead reflects changes in the relative abundance of sediment supplied from Taiwan compared to Luzon, revealing an enhanced inflow of the Kuroshio Current during the mid-late Holocene. Furthermore, millennial-scale variability in the North Pacific Intermediate Water inflow can be traced using changes in magnetic mineralogy and the inflow appears to have been stronger at the end of the last ice age.

1. Introduction

The South China Sea (SCS) is the largest marginal sea of the western Pacific Ocean, and is an ideal location for reconstructing past environmental changes in southeast Asia in response to climate change. The northern SCS is characterized by a broad continental shelf area adjacent to a deep marine basin, which is connected to the Pacific Ocean through the Luzon Strait (Wang et al., 2005; Zhao et al., 2018) (Figure 1). Its ocean currents are influenced by the East Asian monsoon system and the global thermohaline circulation (Wang et al., 2014). Meanwhile, its sedimentary regime is controlled by the large volumes of terrigenous sediment supplied from mainland Asia and adjacent islands (Z. Liu et al., 2016), and subsequently redistributed by surface and deep-water currents (Zhong et al., 2017). As such, sediment transport may be influenced by various systems including (i) the East Asian monsoon system, (ii) long-shore currents, (iii) the branches of the Kuroshio Current that intrude the SCS, (iv) the deep-water currents originating in the Pacific Ocean, and (v) global sea-level changes (Yuan et al., 2014; Zhao et al., 2014) (Figure 1a). However, the interplay of these different processes in terms of their influence on the depositional regime of the northern SCS remains ambiguous in the geological past (Zhang et al., 2022).

A better understanding of the depositional system in the northern SCS is essential if reliable paleoclimatic and paleoceanographic information is to be derived from marine sediments archives. To this end, records from multiple sites, and the integration of multiple proxies that have differing sensitivities to terrestrial weathering and erosion and to sediment transport processes are required (Boulay et al., 2007; Clift et al., 2014; Hu et al., 2012). For example, clay mineralogy has gained particular attention for reconstructing the past evolution of erosion and weathering on the adjacent Asian continent and islands over a range of timescales (Liu et al., 2008; 2009). However, both physical erosion and chemical weathering can change the nature and proportion of different clay minerals available in the source area and/or transported to the ocean through time (Clift et al., 2014; Zhao et al., 2018). The physicochemical properties of magnetic particles, which are produced in the different continental source areas surrounding the SCS, could therefore represent an alternative tracer for changes in the detrital sources (Horng et al., 2012; Horng and Huh, 2011; Huang et al., 2021; Kissel et al., 2016, 2017). In a review, Clift (2016) argued that thermochronology methods make the most effective provenance tools in the SCS because of the changing and overlapping character of many other provenance tracers between potential sources. Alternatively, because magnetic grains are generally less sensitive to weathering than the clay fraction, the combined use of magnetic and clay mineralogy has the potential to provide complementary constraints on the past evolution of monsoon-driven inputs, sediment redistribution, and ocean circulation in this region (Chen et al., 2017; Kissel et al., 2020; Zheng et al., 2016). Hence, the overall goal here is to unmix and distinguish the various processes controlling the multiple proxies to obtain reliable paleoclimatic information.

Understanding the roles of past sea-level variability and provenance change are crucial for disentangling the complex driving mechanisms influencing the sedimentary regime of the northern SCS (Phillips and Slattery, 2006; Weaver et al., 2000). On the one hand, global sea level was ~130 m below modern levels during the Last Glacial Maximum (LGM; ~24-19 ka), leading to different land-sea configurations around the SCS that significantly influenced the inputs of terrigenous matter and its redistribution within the basin (Xiong et al., 2020). Both fluvial transport and ocean circulation were affected by the lower sea level, resulting in different transport and depositional patterns for terrigenous sediment during glacial periods (Zhang et al., 2022; Zhong et al., 2021). On the other hand, the northern SCS is currently dominantly supplied by sediments from the Pearl River, Taiwan, and Luzon (Figure 1b), such that past variability in sediment sourcing could also influence the validity of paleoclimatic proxy interpretations (Liu et al., 2019). Therefore, detrital sediment records from this region will reflect a mixture of signals, including the source effects of changes in continental runoff linked to monsoon rainfall, local and regional oceanic transport pathways, and global sea-level change. However, it remains ambiguous how and to what extent past climatic variability, provenance change, and sea-level change have influenced the sedimentary records from the northern SCS (Zhang et al., 2022).

In order to fully understand the source-to-sink detrital sediment system in the northern SCS, we must consider depositional patterns near estuaries (Hu et al., 2013), near the shore (Li et al., 2015), and within the deep basin (Kaboth-Bahr et al., 2021; Wan et al., 2007; Xu et al., 2021; Zhao et al., 2018). In this study, we analyzed two marine gravity cores that represent a depth transect from the marine continental shelf to the deep ocean basin (Figure 1b), enabling us to constrain the regional depositional regime of the northern SCS and its links to sea level and paleoclimate variability over the past 24,000 years. We combined grain-size analysis, clay mineralogy, and magnetic properties of the sediments to detect changes in the terrigenous sediment composition and provenance, and to assess their controlling factors including (i) sea-level, (ii) the East Asian monsoon, and (iii) regional ocean circulation patterns.

2. Materials and Methods

2.1. Sampling and lithology

We analyzed sediments from two gravity cores collected from the northern SCS shelf and slope region: (i) Core F07 (20°10′1.1″N, 115°44′51.480″E, water depth 800 m) and (ii) Core 16ZB-S11 (hereafter called Core S11; 19°38′27″N, 117°36′14″E, water depth 3038 m) (Figure 1b). Core S11 was retrieved during the "OPEN RESEARCH" cruise in 2016 and Core F07 was collected onboard R/V YUEXIAYUZHI20026 by the science party (South China Sea Institute of Oceanology, Chinese Academy of Sciences) in 2019. The shallower Core F07 is bathed in SCS Intermediate Water while the deeper Core S11 lies within SCS Deep Water (Figure 1a). The sediments at both sites are homogenous and predominantly comprise grey silts and clays, with no obvious hiatuses. For this study, we selected 10 mg of mixed planktonic foraminifera species (*N.dutertrei*, *G. ruber*, *G. sacculifer*) from both sediment cores for accelerator mass spectrometry (AMS) ^{14}C dating, which was conducted at the laboratory of Beta Analytic. Furthermore, samples were taken at 1–3 cm intervals throughout the 3–4 m cores to perform analyses of grain size in Core F07, and clay mineralogy and magnetic mineralogy in both cores.

2.2. Grain size analysis

A sequential procedure was used to extract the detrital fraction from the bulk sediments before grain-size analysis, as follows: (1) carbonate was removed with 1 N HCl at 60°C for 1 h; (2) organic matter was removed with 30% H_2O_2 at 85°C for 1 h; and (3) biogenic silica (including diatoms and radiolarians) was removed with 2 N Na_2CO_3 solution at 85°C for 4 h. The remaining detrital fraction was rinsed with distilled water three times. The grain-size distribution of the detrital fraction was then measured using a Malvern Mastersizer 3000G laser diffraction particle analyzer with a measurement range of 0.01-2000 μm and 0.25 Φ interval resolution. The work was conducted at the Centre for Marine Magnetism (CM^2), Southern University of Science and Technology. The relative standard deviation (RSD) of the measurements is 0.5% and the reproducibility of the instrument is better than 2%. For grain-size analysis, we subsampled Core F07 at 1 cm intervals. Additionally, we used a grain-size end-member (EM) modelling approach (Paterson and Heslop, 2015) to identify the number of theoretical EMs that may have contributed to the sediment and to assess the changing relative proportions of each EM through time (Figure 2).

2.3. Clay mineralogy

Clay mineral analyses were carried out on the <2 µm fraction, which was separated based on Stokes' settling velocity principle and recovered by centrifuging (Dane et al., 2002), following the removal of organic matter and carbonate by treating with hydrogen peroxide (15%) and acetic acid (25%). The extracted clay minerals were smeared on glass slides after being fully dispersed by an ultrasonic bath, and then dried at room temperature. Clay mineral analysis was conducted by X-ray diffraction (XRD) using a D8 ADVANCE diffractometer with CuKα (alpha) radiation (40 kV, 40 mA), at the Key Laboratory of Marine Geology and Environment, Institute of Oceanology, Chinese Academy of Sciences.

Identification of clay minerals was made according to the position of the (001) series of basal reflections on the three XRD diagrams (Moore & Reynolds, 1989). Semi-quantitative estimates of peak areas of the basal reflection for the main clay mineral groups (smectite-17 Å, illite-10 Å, and kaolinite/chlorite-7 Å) were carried out on glycolated samples using Topas 2P software with the empirical factors of Biscaye (1965). Replicate analysis of the same sample produced results with a relative error of ± 5%.

2.4. Magnetic mineral measurements

Volume low- and high-frequency magnetic susceptibility (χ_{lf} and χ_{hf}) were measured at low (976 Hz) and high frequency (15616 Hz) under low fields (200 m/A) using a Kappabridge MFK1-FA (AGICO). Frequency-dependent magnetic susceptibility (χ_{fd}) was calculated from $\chi_{fd} = [(\chi_{lf}-\chi_{hf})/\chi_{lf}] \times 100\%$, and serves as an indicator of the relative content of the ultra-fine magnetic particles close to the superparamagnetic (SP)/single domain (SD) boundary of ferrimagnetic minerals (Oldfield, 1991).

Each sample was subjected to an alternating field (AF) with a peak field of 100 mT and a direct current (DC) bias field of 0.05 mT by a D-2000 AF demagnetizer to obtain the anhysteretic remanent magnetization (ARM), which is regarded as representative of the stable SD ferrimagnetic content (Oldfield, 1991). The susceptibility of anhysteretic remanent magnetization (χ_{ARM}) was obtained from the ARM divided by the DC bias (0.05 mT). Saturation isothermal remanent magnetization (SIRM) was imparted to the Z-axis for each sample with a DC field of 1 T using an IM-10-30 Impulse Magnetizer and was measured on JR-6A Spinner Magnetometer (AGICO). The values of SIRM depend primarily on the content of magnetic minerals and secondarily on the magnetic crystal grain size, but are insensitive to superparamagnetic domains. Subsequently, samples were demagnetized with backfields of -100 and -300 mT, and the corresponding remanence values were measured, termed $IRM_{-100\ mT}$ and $IRM_{-300\ mT}$. The parameter $HIRM_{300mT}$ is defined as $0.5 \times (SIRM_{1.0\ T} + IRM_{-300\ mT})$, and the S-ratio is defined as $-IRM_{-300\ mT}/SIRM_{1.0T}$ (King & Channell, 1991). Analogously, $HIRM_{100\ mT}$ is defined as $0.5 \times (SIRM_{1.0T} + IRM_{-100\ mT})$. $HIRM_{100\ mT}$ and $HIRM_{300\ mT}$ are equivalent to the SIRM after AF demagnetization at 100 mT ($IRM_{@100\ mT}$) and 300 mT ($IRM_{@300\ mT}$), respectively (Q. Liu et al., 2007). χ_{ARM}/SIRM was used to indicate magnetic grain size because it is not affected by superparamagnetic grains. High χ_{ARM}/SIRM values reflect a high content of single-domain grains, whereas low χ_{ARM}/SIRM values reflect coarse magnetic grain sizes (Bloemendal et al., 1992).

3. Results

3.1. Age model

The age model for Core F07 is based on seven AMS ^{14}C ages, while the age model for Core S11 is based on four AMS ^{14}C ages (Table S1). Calendar ages were determined using the MARINE 20 calibration (Heaton et al., 2020) with a regional ^{14}C reservoir age of $\Delta R = 43 \pm 61$ yr (Yang et al., 2020). The resulting linear sedimentation rates (LSR) for both cores are very high, with an average of ~24 cm/kyr for Core F07 (range from 4 to 55 cm/kyr) and ~12 cm/kyr for Core S11 (range from 6 to 23 cm/kyr) (Table S1). The LSRs also display a distinct glacial-interglacial pattern, with four to six times higher sedimentation rates during the LGM compared to the Holocene.

3.2. Grain-size changes and end-member analysis

Sediment from Core F07 comprises clay (4–21%, average 10%), silt (53–85%, average 72%), and sand (1–40%, average 18%) (Figure 2d). The consistent downcore variations in the mean grain size and median grain size are similar to changes in the sand content (Figure 2d).

Grain-size end-member analysis can be used to estimate variations in end-members based on co-variability within a dataset, and is a powerful tool for unmixing grain-size distributions into geologically meaningful end-members (Weltje, 1997). The different end-members and their variations can reflect (1) different controlling mechanisms of sediment transport, (2) sediment supply from different sources, and/or (3) mechanisms which systematically change the grain-size distribution along the transport pathway of the sediment (Boulay et al., 2007; Prins & Postma, 2002). However, it should be noted that these possibilities cannot be distinguished by this mathematical method alone.

For Core F07, both the grain-size distributions of each end-member and their proportional changes through time were quantified based on this method (Figure 2). The goodness of fit statistics (coefficient of determination $R^2 > 0.9$, angular deviation < 5 for three end-members) show that a three end-member model is optimal for Core F07 (Figures 2a and b). This three end-member model contains grain-size modes of 8.23 μm, 40.2 μm, and 74.1 μm for end-members EM1, EM2, and EM3, respectively (Figure 2c). In comparison to traditional classification criteria, the grain sizes of EM 1, EM2, and EM3 are close to fine silt, coarse silt, and fine sand, respectively. The end-member abundances for each end-member since 24 ka are presented in Figure 2d, where it can be seen that EM1 (22–90%, average 47%) is the most significant component and shows an inverse trend through time with EM2 and EM3. In general, the similarity between records of EM3 and the mean grain size suggests that the coarsest end-member EM3 mainly represents nearshore deposits from the Pearl River. The finest EM1 mainly consists of fine-grained, weathered minerals, such as mica, fine quartz, and broken feldspar grains, and was likely influenced by river runoff and weathering changes in response to regional precipitation (Garzanti et al., 2011). Finally, the EM2 component varies in-phase with sea level, consistent with low sea level stands enhancing the regional hydrodynamic force and enabling coarser sediment to be transported to the core site.

3.3. Clay and magnetic mineral results

Southern Taiwan and the Pearl River are the major contributors of sediments to the continental shelf and slope in the northern SCS (Z. Liu et al., 2016), while rivers from Luzon are an additional sediment source in the northeastern part of the basin (Schroeder et al., 2015) (Figure 1b). In the downcore records spanning the last 24 kyr in cores F07 and S11, the clay mineralogy falls along approximately linear arrays between two end-members, one dominated by illite + chlorite and a second dominated by smectite, while kaolinite contents are relatively low (Figure 3). This pattern indicates a mixture of supply from Taiwan (illite and chlorite rich) and Luzon (smectite-rich), with further contributions from South China, likely via the Pearl River (kaolinite-rich, but also some smectite; Hu et al., 2013) (Figure 3). In particular, sediments from East of Pearl River (EPR), including sediment from the Hanjiang River and other local rivers, represents another potential source of smectite (Figure 3) (J. G. Liu et al., 2016; 2019).

Both the EPR and Luzon could be important potential sediment sources for the shallow Core F07, which is located relatively proximal to the Pearl River mouth. In contrast, the clay mineralogy in Core S11 in the deep basin plots close to the Taiwan end-member, similar to Core CS11 (Shen et al., 2022), indicating dominant sourcing from southern Taiwan. Meanwhile, other cores on the northern SCS slope, including ODP Site 1144 (Hu et al., 2012) and Core MD12-3434 (Zhao et al., 2018), record a greater proportion of Luzon-derived sediments (Figure 3). During the LGM, with lowered sea level, it is likely that the sediments in Core F07 were partly derived from the paleo-Pearl River, or the Hanjiang River and other local rivers, given that lowered sea level would have made these inputs more proximal to the site.

In contrast to the glacial-interglacial stability of the kaolinite content in Core S11, the kaolinite content in Core F07 was higher during the glacial period (~11–18%) and peaked during Heinrich Stadial 1 (HS1), before decreasing during the deglaciation to reach stable Holocene values of around 8–10% (Figure 4b). The smectite/(illite + chlorite) ratios in Core F07 varied from 0.2 to 0.5 (Figure 5c), with millennial-scale changes throughout, whereas the ratios in Core S11 ranged from 0.1 to 0.3, with distinctly elevated values during the mid-late Holocene from ~6 to 2 ka (Figure 5e).

The rock magnetic parameters in cores F07 and S11 show similar patterns through time (although different absolute values), with lower S-ratios during the LGM and HS1 (Figure 4c), indicating a relatively higher content of high-coercivity maghemite/hematite than low-coercivity titano-magnetite during these time intervals.

4. Discussion

The geographic extent of the SCS spanning different regional, monsoon-controlled climate regions (Chen et al., 2017), as well as the geological heterogeneity between the different river catchments, leads to different sediment particles being delivered to the SCS from different sources (Clift et al., 2015). Previous studies found complex depositional patterns, influenced by both down-slope and along-slope processes on the continental slope of the northern SCS (Kaboth-Bahr et al., 2021; J. Liu et al., 2017). Such complexity may have been associated with sea-level changes, which could influence the proportions of sediment supplied from different sources to individual sites due to (i) changes in the land-sea configuration, (ii) the varying strength of ocean current activity at different water depths, or (iii) changes in ocean current strength linked to variations in the monsoon winds (C. Liu et al., 2017; Xu et al., 2021). Changes in sediment characteristics could also have been caused by changes in chemical weathering and fluvial sediment discharge driven by climate change. Below, we assess how these processes have influenced the provenance and terrigenous sediment transport in the northern SCS since the LGM, before exploring what the records reveal about past changes in the monsoonal inputs and regional oceanography.

4.1. Provenance and transport processes forced by glacial sea-level change

During the LGM, when the sea level was about 130 m lower than today (Wang et al., 2014) (Figure 4a), the reduced distance between river mouths and the core sites could have influenced the clay mineralogy and the sediment magnetic properties. That suggestion is supported by the observed co-variations of kaolinite/illite ratios in Core F07 and other cores from the northern SCS slope (e.g., GeoB16602-4; J. Liu et al., 2017) (Figure 4b) with sea-level (Figure 4a). Those records indicate that the Pearl River (and possibly the EPR) became a more significant source to these sites during the LGM (Figure 3), and probably also acted as the dominant contributor of the coarse sediment at this time (Figure 4d). Moreover, coastline migration and changes in seasonality linked to sea-level fall could have enhanced the reworking of previously deposited sediments from the exposed shelves (C. Liu et al., 2017; J. Liu et al., 2017). In sum, both the reduced distance from land and increased sediment reworking could have led to an enhancement in local sediment supply from the South China margin, which is also reflected in the depositional rates in the SCS cores (Table S1).

The shallower Core F07 was characterized by a relatively greater contribution of kaolinite compared to illite during the LGM (Figure 4b), suggesting an enhanced influence from Pearl River (or EPR) sources at that time (Figure 2), while the deep-water Core S11 had a similar kaolinite/illite ratio during both the LGM and the Holocene (Figure 4b). Hence, the clay mineral assemblages in this region were controlled by both water depth and sediment transport pathways, with deglacial sea-level change appearing to have influenced the relative contribution of reworked sediment from the Pearl River catchment to shallow-water sites but not to sites in the deep basin (Figure 6a). Sea-level fall and the associated mesoscale eddies during the LGM appear to have enhanced the supply of kaolinite from the Pearl River and its relict sediments on the continental shelf to the open ocean, leading to enhanced accumulation at shallower sites. However, the majority of the kaolinite was not exported to the deep basin (Cao et al., 2019, 2021) (Figure 6a). Moreover, increased sediment exposure and subsequent silicate weathering could also have supplied tropical shelf sediments, including minerals such as kaolinite, to the shallow sites during glacial lowstands (Wan et al., 2017).

The magnetic fraction in sediments from the northern SCS can also be used to trace provenance, based on the modern regional differences in the river-borne magnetic properties (Figure 1b). The S-ratio of surficial sediments is lower in the Mekong River (0.79) and Red River (0.87) than in the Pearl River (0.90) and Taiwanese rivers (0.96) (Table S2), which indicates relatively higher hematite contents for the sediment supplied to the western and southern SCS than to the northern SCS (Kissel et al., 2016, 2017). Based on comparison to those fluvial sources, the relatively high values for χ_{lf}, χ_{ARM}, SIRM, and S-ratio in cores F07 and S11 indicate a high abundance of fine-grained magnetite from northern sources mixed with minor amounts of hematite, probably from Pearl River sources (Table S2). Compared to the relatively high S-ratio in both the studied cores, a significant decrease in S-ratio occurred during the last glacial interval at other sites in the SCS, including Core PC338 in the northwestern SCS (M. Li et al., 2018a) and Core B9 in the southern SCS (Zhong et al., 2021) (Figure 4c). These lower

S-ratio in the northwestern and southern SCS indicate an increase in the relative proportion of hematite, which may have been supplied as aerosol dust (Chen et al., 2017) or as strong weathering inputs (Yang et al., 2016). While it seems that sediments sourced from the Red and Mekong rivers lowered the S-ratio at those sites during the last glacial interval, evidently those inputs did not affect the cores in the northern SCS. In this context, the preservation of the modern north-south gradient in the S-ratio (Figure 4c) further indicates the dominant influence of local continental sources of magnetic particles in each basin. However, we also note that in some particular intervals, changes in the East Asian winter monsoon and the related winter coastal current could also have influenced the hematite content in this region (M. Li et al., 2018a).

In general, sea-level changes during the LGM could regulate and control the clay and magnetic mineral records from shallow-water sites by influencing the incision of rivers on the shelves and sediment storage near the river mouths, and might also be expected to affect the grain size (Figure 4d). Specifically, an increased proportion of the coarser silt grain-size component (EM2) and an increased magnetic grain size in the shallow Core F07 (Figure 2d, Figure 4d) suggest preferential sourcing and/or transport of this fraction during the interval of lowered sea-level. However, based on differences in the sedimentation rate between cores F07 and S11 (Table S1), and differences in the timing of the deglacial changes in grain size (Figures 4d and e), we suggest that the glacial coarsening in magnetic particles in the deep-water Core S11 (Figure 4e) was driven by a different oceanographic mechanism, such as changes in contour currents (Wang et al., 2020) or mesoscale eddies (Cao et al., 2021) (Figure 6a). Furthermore, our data are consistent with the hypothesis that the magnetic grain size of SCS cores could record the flow strength of deep water inflow from the North Pacific (Zheng et al., 2016).

4.2. Impacts of deep-water circulation during the deglacial cold periods

The oceanographic connection between the North Pacific and the SCS makes this marginal sea an ideal location in which to reconstruct the past evolution of North Pacific Intermediate Water (NPIW) and to assess any links with millennial-scale climate variability during the last deglaciation (~19–11 ka) (Huang et al., 2013; G. Li et al., 2018). During the last deglaciation, major meltwater discharges reduced North Atlantic surface water density and may have weakened the Atlantic meridional overturning circulation (AMOC) during HS1 and perhaps the Younger Dryas (McManus et al., 2004). Through atmospheric and oceanic teleconnections, the effects of the reorganization of poleward heat flow in the North Atlantic are proposed to have extended to the North Pacific, leading to deep-water formation occurring in the North Pacific between ~17 and 15 ka (Okazaki et al., 2010). Such a major rearrangement of the Pacific circulation might be expected to have left a signal in the northern SCS.

We identify an intensification of the magnetic grain size signature in cores S11 (Figure 4e) and 10E203 (Figure 4f) (Zheng et al., 2016) during HS1 and the Younger Dryas. This hydrodynamic signature can be associated with the flow of the deep-water currents in the SCS (Figure 1b, Figure 6b). Notably, these changes were approximately synchronous with weakening of the Atlantic meridional overturning circulation (Figure

4g) (McManus et al., 2004), and coincident with regional circulation changes in the North Pacific, such as increases in NPIW formation in the North Pacific (Figure 4h) (Horikawa et al., 2021), which supports the above hypothesis.

Previous studies have suggested that NPIW formation in the subarctic Pacific Ocean was more intense during the last glacial period (Rae et al., 2020; Rella et al., 2012) and/or during HS1 (Gong et al., 2019; Okazaki et al., 2010). Evidence for enhanced NPIW formation is also found in neodymium isotope shifts at Site MD01-2420 in the northwestern Pacific Ocean (Figure 4h) (Horikawa et al., 2021), with less radiogenic values concurrent with the younger ^{14}C ventilation ages during cold intervals (Okazaki et al., 2010). Neodymium isotopes represent a tracer for water mass provenance, so these records specifically support water mass formation in the Okhotsk and/or Bering Seas (Horikawa et al., 2010). The simulated deep-water pathways extend southwards along the western margin of the North Pacific, and consequently should influence the Philippine Sea and the northern SCS (Wan & Jian, 2014), making these deep-water core sites (Figure 4e and f) sensitive locations for tracing these changes. Whereas such abrupt changes in NPIW influenced the magnetic fraction in the northern SCS during the last deglaciation (Figure 6b), significant circulation changes do not appear to have occurred during the Holocene period (Figure 4e and f), consistent with the relative stability in high-latitude climate records from this interval (Figure 4i) (North Greenland Ice Core Project members, 2004).

4.3. Impacts of the East Asian summer monsoon during deglacial and Holocene periods

During the deglacial and interglacial warm periods, enhanced summer precipitation was associated with a stronger East Asian summer monsoon (EASM) (Figure 5a). Enhanced river discharges evidently impacted sediment supply rates, as recorded by Ti/Ca ratios in Core ORI-P1 from the northeastern SCS (Kaboth-Bahr et al., 2021). Clay mineral formation in both Taiwan and Luzon is also strongly controlled by the higher temperatures and heavier rainfall under an enhanced EASM Z. Liu et al., 2007), but the input processes to the SCS may have differed between those two islands. The steep and narrow shelf of the southwestern Taiwan margin means that sediments from Taiwan are transported rapidly from river catchments to the deep northern SCS basin via submarine canyons (J. T. Liu et al., 2016). In contrast, sediments from northern Luzon rivers are first carried into the shallow Luzon Strait, before being transported to the northern SCS by surface ocean currents. Therefore, in addition to the EASM system, the evolution of the oceanic circulation may be an important factor that determines the supply of fine-grained sediment to the northern SCS basin.

The supply of illite and chlorite from Taiwan is the product of rainfall-driven erosion, while the supply of smectite from Luzon depends on both rapid chemical weathering and physical erosion (Liu et al., 2009). In addition, the weathering of volcanic rocks under a hot humid climate in the EPR area can also generate smectite (Liu et al., 2019). Therefore, the smectite/(illite + chlorite) ratios in Core F07 can be taken to indicate changes in the monsoon precipitation in Luzon and/or South China (Figure 6c).

Increases in smectite/(illite + chlorite) ratios in Core F07 during during the Early Holocene and possibly the Bølling-Allerød interstadial (Figure 5c) could reflect strengthened weathering and/or recycling of older sediments due to EASM rainfall (Figure 5a) (Colin et al., 2010; Zhao et al., 2018), similar to what is seen at ODP Site 1144 (Hu et al., 2012) This record also shows some similarities to changes in specific grain-size components in cores F07 and PC338 (M. Li et al., 2018b) from the northwestern SCS (Figure 5b); increased fine-grained fluvial material that was presumably transported in suspension by northern SCS surface water currents could potentially reflect increased terrestrial erosion linked to enhanced precipitation (M. Li et al., 2018b). As a corollary, decreases in both the smectite/(illite + chlorite) ratios (Figure 5c) and the proportions of fine-grained sediment (Figure 5b) during HS1 coincided with a weakened EASM (Figure 5a) (Wang et al., 2008). These fluctuations are also consistent with shifts in the position of the mean summer Intertropical Convergence Zone (ITCZ) (Figure 5h) (Tachikawa et al., 2011). A southward shift in the ITCZ during HS1 would have reduced the regional precipitation and reduced the erosion of chemically-weathered sediments on the shelf. Interestingly, a signal of the EASM intensity is also recognized in several other sites from a range of water depths in the northern SCS, including cores MD05-2904 (Liu et al., 2010) (Figure 5d) and MD12-3434 (Zhao et al., 2018). These oscillations indicate the rapid response of terrigenous sediment inputs, recycling, and provenance in the low-latitude SCS to variations in monsoonal rainfall (Cheng et al., 2016; Clift, 2020; Zhao et al., 2018).

4.4. Effect of the Kuroshio Current strength during the Mid-late Holocene

In contrast to the clay mineral records from the shallow-water sites that were dominated by monsoonal inputs (Figures 5c and d), our clay mineral reconstruction from the deep-water Core S11 (Figure 5e) does not resemble monsoonal variations (Figure 5a). We therefore suggest that neither the EASM monsoonal-forced inputs nor the EASM monsoonal-forced surface currents had a significant impact on the relative supply to the deep basin of smectite from Luzon (or possibly the EPR) compared to illite and chlorite from Taiwan. Instead, the synchronous mid-late Holocene increase in smectite/(illite + chlorite) in deep-water cores S11 and CS11 (Shen et al., 2022) (Figures 5e and f) indicates an increase in the Luzon contribution (or possibly the Pearl River or EPR) relative to Taiwan, which suggests a link to an enhanced Kuroshio Current intrusion during the mid-late Holocene (Z. Liu et al., 2016).

A comparison of those clay mineral records (Figures 5e and f) to the trends in both the warm-water diatom species from ODP Site 1144 (Jiang et al., 2006) (Figure 5f) and Kuroshio Current intensity proxies from the Okinawa Trough (Zheng et al., 2014) supports the hypothesis that intrusion of the Kuroshio Current influenced the transport of Luzon-derived clay minerals to the deep basin (Z. Liu et al., 2016) (Figure 6d). The large-scale tropical Pacific atmospheric circulation is thought to be an important driver of the decadal-scale intrusion of the Kuroshio Current (Chen et al., 2020). Hence, the strong intensity of the Kuroshio intrusion during the mid to late Holocene may have been related to the evolution of the East Asian winter monsoon (Figure 5g) (Kang et al., 2020), driven itself by changes in high-latitude Northern Hemisphere ice volume and mid- to high-latitude Northern Hemisphere atmospheric temperatures (Ding et al., 2022).

In summary, we provide evidence that the evolution of the regional ocean circulation is an important factor determining the fine-grained sediment supply and dispersion beyond the continental margins during warm periods with high sea-level stands (Figure 6c and d). Therefore, clay mineralogy may be a useful tool for reconstructing the past dynamics in these systems at such times. Specifically, our data support the idea that the strength of the Kuroshio Current intrusion into the SCS could influence the transport of clay fractions from Luzon into deep-water settings of the basin under the influence of the East Asian winter monsoon (Figure 6d).

5. Conclusions

We conducted a high-resolution study of grain size, clay mineralogy, and magnetic mineral properties on two sediment cores representing a depth transect in the northern SCS. Combined with other lines of evidence on regional hydroclimate and Pacific ocean-atmosphere dynamics, we assessed the influence of changes in sea level, deep and surface ocean currents, and the EASM system on the sedimentary proxies. Firstly, low sea-level during the LGM led to elevated fluxes of kaolinite and magnetic minerals from the Pearl River and its exposed shelf, but these mostly accumulated on the shallow margin rather than influencing the deeper northern SCS basin, which was more strongly affected by sediment fluxes from Taiwan. Secondly, changes in magnetic grain size indicate that there was a stronger deep-water current in the northern SCS during HS1 and the Younger Dryas, which may reflect enhanced formation of North Pacific intermediate or deep waters. Thirdly, fluctuations in smectite/(illite + chlorite) ratios at the shallow margin site coincided with the deglacial millennial-scale evolution of the EASM, suggesting enhanced weathering and/or reworking of weathered sediment controlled by a stronger summer monsoon. Finally, such deglacial changes in clay mineralogy are not seen in cores from the deep basin, which instead record distinct mid-late Holocene increases in smectite/(illite + chlorite) ratios, consistent with an intensification of the Kuroshio Current intrusion that led to an enhanced supply of Luzon-derived sediments to the open northern SCS. Overall, our work gives new insights into the roles of varying terrestrial weathering and oceanographic processes in controlling the depositional record on the northern SCS margin correlating to climatic and sea-level fluctuations.

Open Research

Data acuqired during this study is available at Zenodo (Zhong, 2022).

Acknowledgements

The authors thank Yutian Xuan (South China Sea Institute of Oceanology, Chinese Academy of Sciences) for helpful sampling analysis. The authors also thank Ursula Röhl, Mingkun Li, and an anonymous reviewer for their insightful input which helped us to improve the final manuscript. This work was supported financially by the National Natural Science Foundation of China (grant 42274094, 92158208, 42261144739, 41976065), Natural Science Foundation of Guangdong Province (2021A1515011370), the State Key Laboratory of Marine Geology, Tongji University (No. MGK202209), the opening foundation (SSKP202101) of the Shanghai Sheshan National Geophysical Observatory (Shanghai, China), the State Key Laboratory of Marine Geology, Shenzhen Science and Technology Program (KQTD20170810111725321), the Fundamental Research Funds for National University, China University of Geosciences (Wuhan), and a NERC independent research fellowship (NE/T011440/1) to DJW. For the purpose of open access, the author has applied a “Creative Commons Attribution (CC BY) license” to any Author Accepted Manuscript version arising.

References

Biscaye, P. E. (1965). Mineralogy and Sedimentation of Recent Deep-Sea Clay in the Atlantic Ocean and Adjacent Seas and Oceans. *GSA Bulletin*, *76*, 803–832.

Bloemendal, J., King, J. W., Hall, F. R., & Doh, S. J. (1992). Rock magnetism of Late Neogene and Pleistocene deep-sea sediments: Relationship to sediment source, diagenetic processes, and sediment lithology. *Journal of Geophysical Research: Solid Earth*, *97*, 4361–4375.

Boulay, S., Colin, C., Trentesaux, A., Clain, S., Liu, Z. F., & Lauer-Leredde, C. (2007). Sedimentary responses to the Pleistocene climatic variations recorded in the South China Sea. *Quaternary Research*, *68*, 162–172.

Cao, L., Liu, J., Shi, X., He, W., & Chen, Z. (2019). Source-to-sink processes of fluvial sediments in the northern South China Sea: Constraints from river sediments in the coastal region of South China. *Journal of Asian Earth Sciences*, *185*, 104020.

Cao, L., Liu, J., Xu, X., Qiao, Y., Khan, M. H. R., & Tan, L. (2021). The influence of mesoscale eddies on sedimentary processes in the western South China Sea since 32 kyr BP. *Marine Geology*, *441*, 106621.

Chen, Q., Kissel, C., & Liu, Z. (2017). Late Quaternary climatic forcing on the terrigenous supply in the northern South China Sea: Input from magnetic studies. E*arth and Planetary Science Letters*, *471*, 160–171.

Chen, Y. C., Zhai, F. G., & Li, P. L. (2020). Decadal Variation of the Kuroshio Intrusion Into the South China Sea During 1992-2016. *Journal of Geophysical Research: Oceans*, *125*, e2019JC015699.

Cheng, H., Edwards, R. L., Sinha, A., Spötl, C., Yi, L., & Chen, S. (2016). The Asian monsoon over the past 640,000 years and ice age terminations. *Nature*, *534*, 640–646.

Clift, P. D., Brune, S., & Quinteros, J. (2015). Climate changes control offshore crustal structure at South China Sea continental margin. *Earth and Planetary Science Letters*, *420*, 66–72.

Clift, P. D., Wan, S., & Blusztajn, J. (2014). Reconstructing chemical weathering, physical erosion and monsoon intensity since 25 Ma in the northern South China Sea: A review of competing proxies. *Earth-Science Reviews*, *130*, 86–102.

Clift, P. D. (2020). Asian monsoon dynamics and sediment transport in SE Asia. *Journal of Asian Earth Sciences*, *195*, 104352.

Clift, P. D. (2016). Assessing effective provenance methods for fluvial sediment in the South China Sea. In: Clift, P. D., Harff, J., Wu, J., Qui, Y. (Eds.), River-dominated shelf sediments of East Asian seas. Special Publication, 429, *Geologcial Society, London*, pp. 9–29.

Colin, C., Siani, G., Sicre, M.A., & Liu, Z. (2010). Impact of the East Asian monsoon rainfall changes on the erosion of the Mekong River basin over the past 25,000yr. *Marine Geology*, *271*, 84–92.

Dane, J. H., Topp, C., Campbell, G. S., Horton, R., Jury, W. A., & Nielsen, D. R. (2002). *Part 4. Physical Methods, Methods of Soil Analysis*, Soil Sci. Soc. of Am., Madison, Wis.

Dadson, S. J., Hovius, N., Chen, H., Dade, W. B., Hsieh, M. L., Willett, S. D., et al.

(2003). Links between erosion, runoff variability and seismicity in the Taiwan orogen. *Nature*, *426*, 648-651.

Ding, X., Hu, B. Q., Li, J., Zhao, J. T., Yao, Y., Li, Q., Lan, J. H., et al. (2022). Late Holocene Orbital Forcing and Solar Activity on the Kuroshio Current of Subtropical North Pacific at Different Timescales. *Frontiers in Earth Science*, *10*, 845228.

Garcia, H. E., Locarnini, R. A., Boyer, T. P., Antonov, J. I., Baranova, O. K., Zweng, M. M., et al. (2014). In S. Levitus, & A. Mishonov (Eds.), *World Ocean Atlas 2013, Volume 3: Dissolved Oxygen, Apparent Oxygen Utilization, and Oxygen Saturation* (Vol. 75, pp. 1–27). Silver Spring, MD: NOAA Atlas NESDIS.

Grant, K. M., Rohling, E. J., Ramsey, C. B., Cheng, H., Edwards, R. L., Florindo, F., et al. (2014). Sea-level variability over five glacial cycles. *Nature Communications*, *5*, 5076–5079.

Garzanti, E., Andó, S., France-Lanord, C., Censi, P., Vignola, P., Galy, V., Lupker, M. (2011). Mineralogical and chemical variability of fluvial sediments 2. Suspended-load silt (Ganga-Brahmaputra, Bangladesh). *Earth Planetary Science Letter*, *302*, 107–120.

Gong, X., Lembke-Jene, L., Lohmann, G., Knorr, G., Tiedemann, R., Zou, J. J., et al. (2019). Enhanced North Pacific deep-ocean stratification by stronger intermediate water formation during Heinrich Stadial 1. *Nature Communications*, *10*, 656.

Hanebuth, T., Stattegger, K., & Grootes, P. M. (2000). Rapid flooding of the Sunda Shelf: A late-glacial sea-level record. *Science*, *288*(5468), 1033–1035.

Heaton, T. J., Koehler, P., Butzin, M., Bard, E., Reimer, R. W., Austin, W. E. N., et al. (2020). Marine20-The marine radiocarbon age calibration curve (0-55,000 Cal BP). *Radiocarbon*, *62*, 779–820.

Horikawa, K., Asahara, Y., Yamamoto, K., & Okazaki, Y. (2010). Intermediate water formation in the Bering Sea during glacial periods: Evidence from neodymium isotope ratios. *Geology*, *38*(5), 435–438.

Horikawa, K., Kozaka, Y., Okazaki, Y., Sagawa, T., Onodera, J., Asahi, H., et al. (2021). Neodymium Isotope Records From the Northwestern Pacific: Implication for Deepwater Ventilation at Heinrich Stadial 1. *Paleoceanography and Paleoclimatology*, *36*, e2021PA004312.

Horng, C.-S., Huh, C.-A., Chen, K.-H., Lin, C.-H., Shea, K.-S., & Hsiung, K.-H. (2012). Pyrrhotite as a tracer for denudation of the Taiwan orogen. *Geochemistry, Geophysics, Geosystems*, *13*(8), Q08Z47.

Horng, C.S., & Huh, C.A. (2011). Magnetic properties as tracers for source-to-sink dispersal of sediments: A case study in the Taiwan Strait. *Earth and Planetary Science Letters*, *309*, 141–152.

Hu, D., Böning, P., Köhler, C. M., Hillier, S., Pressling, N., Wan, S., et al. (2012). Deep sea records of the continental weathering and erosion response to East Asian monsoon intensification since 14ka in the South China Sea. *Chemical Geology*, *326*, 1–18.

Hu, D., Clift, P. D., Böning, P., Hannigan, R., Hillier, S., Blusztajn, J., et al. (2013). Holocene evolution in weathering and erosion patterns in the Pearl River delta.

Geochemistry, Geophysics, Geosystems, *14*, 2349–2368.

Huang, J., Jiao, W., Liu, J., Wan, S., Xiong, Z., Zhang, J., et al. (2021). Sediment distribution and dispersal in the southern South China Sea: Evidence from clay minerals and magnetic properties. *Marine Geology*, *439*, 106560.

Huang, K.-F., You, C.-F., Chung, C.-H., Lin, Y.-H., & Liu, Z. (2013). Tracing the Nd isotope evolution of North Pacific Intermediate and Deep Waters through the last deglaciation from South China Sea sediments. *Journal of Asian Earth Sciences*, *79*, 564–573.

Jiang, H., Björck, S., Ran, L., Huang, Y., & Li, J. (2006). Impact of the Kuroshio Current on the South China Sea based on a 115 000 year diatom record. *Journal of Quaternary Science*, *21*, 377–385.

Kaboth-Bahr, S., Bahr, A., Yamoah, K.A., Chuang, C.-K., Li, H.-C., Su, C.-C., et al. (2021). Rapid humidity changes across the Northern South China Sea during the last ~40 kyrs. *Marine Geology*, *440*, 106579.

Kang, S. G., Du, J. H., Wang, N., Dong, J. B., Wang, D., Wang, X. L., Qiang, X. K., et al. (2020). Early Holocene weakening and mid- to late Holocene strengthening of the East Asian winter monsoon. *Geology*, *48*, 1043–1047.

King, J. W., & Channell, J. E. T. (1991). Sedimentary magnetism, environment magnetism, and magnetostratigraphy. *Rev. Geophys*, *29*, 358–370.

Kissel, C., Laj, C., Jian, Z., Wang, P., Wandres, C., & Rebolledo-Vieyra, M. (2020). Past environmental and circulation changes in the South China Sea: Input from the magnetic properties of deep-sea sediments. *Quaternary Science Reviews*, *236*, 106263.

Kissel, C., Liu, Z., Li, J., & Wandres, C. (2016). Magnetic minerals in three Asian rivers draining into the South China Sea: Pearl, Red, and Mekong Rivers. *Geochemistry, Geophysics, Geosystems*, *17*, 1678–1693.

Kissel, C., Liu, Z., Li, J., & Wandres, C. (2017). Magnetic signature of river sediments drained into the southern and eastern part of the South China Sea (Malay Peninsula, Sumatra, Borneo, Luzon and Taiwan). *Sedimentary Geology*, *347*, 10–20.

Lambeck, K., Rouby, H., Purcell, A., Sun, Y., & Sambridge, M. (2014). Sea level and global ice volumes from the Last Glacial Maximum to the Holocene. *Proceedings of the National Academy of Sciences*, *111*, 15296–15303.

Laskar, J., Robutel, P., Joutel, F., Gastineau, M., Correia, A. C. M., & Levrard, B. (2004). A long-term numerical solution for the insolation quantities of the Earth. *Astronomy & Astrophysics*, *428*(1), 261–285.

Li, G., Yan, W., Zhong, L., Xia, Z., & Wang, S. (2015). Provenance of heavy mineral deposits on the northwestern shelf of the South China Sea, evidence from single-mineral chemistry. *Marine Geology*, *363*, 112–124.

Li, G., Rashid, H., Zhong, L., Xu, X., Yan, W., & Chen, Z. (2018). Changes in Deep Water Oxygenation of the South China Sea Since the Last Glacial Period. *Geophysical Research Letters*, *45*, 2018GL078568.

Li, M., Ouyang, T., Roberts, A.P., Heslop, D., Zhu, Z., Zhao, X., et al. (2018a). Influence of sea level change and centennial East Asian monsoon variations on northern South China Sea sediments over the past 36 kyr. *Geochemistry*

Geophysics Geosystems, *19*, 1674–1689.

Li, M., Ouyang, T., Tian, C., Zhu, Z., Peng, S., Tang, Z., et al. (2018b). Sedimentary responses to the East Asian monsoon and sea level variations recorded in the northern South China Sea over the past 36 kyr. *Journal of Asian Earth Sciences*, *171*, 213–224.

Liu, C., Clift, P. D., Carter, A., Böning, P., Hu, Z., Sun, Z., et al. (2017). Controls on modern erosion and the development of the Pearl River drainage in the late Paleogene. *Marine Geology*, *394*, 52–68.

Liu, J. G., Xiang, R., Chen, M. H., Chen, Z., Yan, W., & Liu, F. (2011). Influence of the Kuroshio current intrusion on depositional environment in the northern South China Sea: evidence from surface sediment records. *Marine Geology*, *285*, 59-68.

Liu, J. G., Xiang, R., Kao, S. J., Fu, S. Y., & Zhou, L. P. (2016). Sedimentary responses to sea-level rise and Kuroshio Current intrusion since the Last Glacial Maximum: Grain size and clay mineral evidence from the northern South China Sea slope. *Palaeogeography, Palaeoclimatology, Palaeoecology*, *450*, 111–121.

Liu, J. G., Steinke, S., Vogt, C., Mohtadi, M., De Pol-Holz, R., & Hebbeln, D. (2017). Temporal and spatial patterns of sediment deposition in the northern South China Sea over the last 50,000 years. *Palaeogeography, Palaeoclimatology, Palaeoecology*, *465*, Part A, 212–224.

Liu, J. G., Cao, L., Yan, W., Shi, X. F., et al., (2019). New archive of another significant potential sediment source in the South China Sea. *Marine Geology*, *410*, 16–21.

Liu, J. P., Milliman, J. D., Gao, S., & Cheng, P. (2004). Holocene development of the

Yellow River's subaqueous delta, North Yellow Sea. *Marine Geology*, *209*(1), 45–67.

Liu, J. T., Hsu, R. T., Hung, J. J., Chang, Y. P., Wang, Y. H., Rendle-Bühring, R. H., et al. (2016). From the highest to the deepest: The Gaoping River–Gaoping Submarine Canyon dispersal system. *Earth-Science Reviews*, *153*, 274–300.

Liu, Q., Roberts, A. P., Torrent, J., Horng, C. S., & Larrasoaña, J. C. (2007). What do the HIRM and S-ratio really measure in environmental magnetism? *Geochemistry, Geophysics, Geosystems*, *8*, Q0911.

Liu, Y. L., Gao, S., Wang, Y. P., Yang, Y., Long, J. P., Zhang, Y. Z., et al. (2014). Distal mud deposits associated with the Pearl River over the northwestern continental shelf of the South China Sea. *Marine Geology*, *347*, 43-57.

Liu, Z., Li, X., Colin, C., & Ge, H. (2010). A high-resolution clay mineralogical record in the northern South China Sea since the Last Glacial Maximum, and its time series provenance analysis. *Chinese Science Bulletin*, *55*, 4058–4068.

Liu, Z., Tuo, S., Colin, C., Liu, J. T., Huang, C. Y., Selvaraj, K., et al. (2008). Detrital fine-grained sediment contribution from Taiwan to the northern South China Sea and its relation to regional ocean circulation. *Marine Geology*, *255*, 149–155.

Liu, Z., Zhao, Y., Colin, C., Siringan, F. P., & Wu, Q. (2009). Chemical weathering in Luzon, Philippines from clay mineralogy and major-element geochemistry of river sediments. *Applied Geochemistry*, *24*, 2195–2205.

Liu, Z., Zhao, Y., Colin, C., Stattegger, K., Wiesner, M. G., Huh, C. A., et al. (2016). Source-to-Sink transport processes of fluvial sediments in the South China Sea.

Earth-Science Reviews, *153*, 238–273.

Liu, Z., Colin, C., Huang, W., Le, K. P., Tong, S. Q., Chen, Z., et al. (2007). Climatic and tectonic controls on weathering in south China and Indochina Peninsula: Clay mineralogical and geochemical investigations from the Pearl, Red, and Mekong drainage basins. *Geochemistry, Geophysics, Geosystems*, *8*(5), Q05005.

McManus, J. F., Francois, R., Gherardi, J. M., Keigwin, L. D., Brown-Leger, S. (2004). Collapse and rapid resumption of Atlantic meridional circulation linked to deglacial climate changes. *Nature*, *428*, 834–837.

Milliman, J. D., & Meade, R. H. (1983). World wide delivery of river sediment to the oceans. *Journal of Geology*, *91*(1), 1–21.

Moore, D. M., & Reynolds, R. C. (1989). X-ray Diffraction and the Identification and Analysis of Clay Minerals, Oxford Univ. Press, Oxford.

North Greenland Ice Core Project members. (2004). High-resolution record of Northern Hemisphere climate extending into the last interglacial period. *Nature*, *43*, 147–151.

Okazaki, Y., Timmermann, A., Menviel, L., Harada, N., Abe-Ouchi, A., Chikamoto, M. O., et al. (2010). Deepwater Formation in the North Pacific During the Last Glacial Termination. *Science*, *329*, 200–204.

Oldfield, F. (1991). Environmental magnetism — A personal perspective. *Quaternary Science Reviews*, *10*, 73–85.

Paterson, G.A., & Heslop, D. (2015). New methods for unmixing sediment grain size data. *Geochemistry Geophysics Geosystems*, *16*, 4494–4506.

Phillips, J.D., Slattery, M.C. (2006). Sediment storage, sea level, and sediment delivery to the ocean by coastal plain rivers. *Progress in Physical Geography*, *30*, 513–530.

Prins, M. A., & Postma, G. (2002). Effects of climate, sea level, and tectonics unraveled for last deglaciation turbidite records of the Arabian Sea. *Geology*, *28*, 375–378.

Qu, T. D., Du, Y., & Sasaki, H. (2006). South China Sea throughflow: A heat and freshwater conveyor. *Geophysical Research Letters*, *332*(23), 430-452.

Rae, J. W. B., Gray, W. R., Wills, R. C. J., Eisenman, I., Fitzhugh, B., Fotheringham, M., et al. (2020). Overturning circulation, nutrient limitation, and warming in the Glacial North Pacific. *Science Advances*, *6*, eabd1654.

Rella, S. F., Tada, R., Nagashima, K., Ikehara, M., Itaki, T., Ohkushi, K.I., et al. (2012). Abrupt changes of intermediate water properties on the northeastern slope of the Bering Sea during the last glacial and deglacial period. *Paleoceanography*, *27*, PA3203.

Schlitzer, R. (2002). Interactive analysis and visualization of geoscience data with Ocean Data View. *Computers & Geosciences*, *28*, 1211–1218.

Schroeder, A., Wiesner, M. G., Liu, Z. (2015). Fluxes of clay minerals in the South China Sea. *Earth and Planetary Science Letters*, *430*, 30–42.

Shaw, P. T., & Chao, S. Y. (1994). Surface circulation in the South China Sea. *Deep Sea Research Part I: Oceanographic Research Papers*, *41*(11), 1663-1683.

Shen, X., Hu, B., Yan, H., Dodson, J., Zhao, J., Li, J., et al. (2022). Reconstruction of Kuroshio intrusion into the south China sea over the last 40 kyr. *Quaternary Science Reviews*, *290*, 107622.

Tachikawa, K., Cartapanis, O., Vidal, L., Beaufort, L., Barlyaeva, T., Bard E. (2011). The precession phase of hydrological variability in the Western Pacific Warm Pool during the past 400 ka. *Ouaternary Science Reviews*, *30*, 3716–3727.

Tian, J. W., Yang, Q. X., Liang, X. F., Xie, L. L., Hu, D. X., Wang, F., et al. (2006). Observation of Luzon Strait transport. *Geophysical Research Letters*, *33*(19), L19607.

Wan, S., & Jian, Z. (2014). Deep water exchanges between the South China Sea and the Pacific since the last glacial period. *Paleoceanography*, *29*, 1162–1178.

Wan, S., Li, A., Clift, P.D., & Stuut, J.-B.W. (2007). Development of the East Asian monsoon: Mineralogical and sedimentologic records in the northern South China Sea since 20 Ma. *Palaeogeography, Palaeoclimatology, Palaeoecology*, *254*, 561–582.

Wan, S., Clift, P. D., Zhao, D. B., Hovius, N., Munhoven, G., France-Lanord, C., et al. (2017). Enhanced silicate weathering of tropical shelf sediments exposed during glacial lowstands: A sink for atmospheric CO_2. *Geochimica et Cosmochimica Acta*, *200*, 123–144.

Wang, P., Clemens, S., Beaufort, L., Braconnot, P., Ganssen, G., Jian, Z., et al. (2005). Evolution and variability of the Asian monsoon system: state of the art and outstanding issues. *Quaternary Science Reviews*, *24*, 595–629.

Wang, P., Li, Q., & Tian, J. (2014). Pleistocene paleoceanography of the South China Sea: Progress over the past 20 years. *Marine Geology*, *352*, 381–396.

Wang, X., Wang, Y., Tan, M., & Cai, F. (2020). Deep-water deposition in response to sea-level fluctuations in the past 30 kyr on the northern margin of the South China Sea. *Deep Sea Research Part I: Oceanographic Research Papers*, *163*, 103317.

Wang, Y., Cheng, H., Edwards, R., Kong, X., Shao, X., Chen, S., et al. (2008). Millennial- and orbital-scale changes in the East Asian monsoon over the past 224,000 years. *Nature*, *451*, 1090.

Weaver, P. P. E., Wynn, R. B., Kenyon, N. H., Evan, J. (2000). Continental margin sedimentation, with special reference to the north-east Atlantic margin. *Sedimentology*, *47*, 239–256.

Weltje, G. (1997). End-member modeling of compositional data: Numerical-statistical algorithms for solving the explicit mixing problem. *Mathematical Geology*, *29*(4), 503–549.

Wu, C. R., 2013. Interannual modulation of the pacific decadal oscillation (PDO) on the low-latitude western North Pacific. *Progress in Oceanography*, *110*, 49-58.

Xiong, P., Harff, J., Xie, X., Zhang, W., Chen, H., Tao, J., et al. (2020). Modeling paleogeographic scenarios of the last glacial cycle as a base for source-to-sink studies: An example from the northwestern shelf of the South China Sea. *Journal of Asian Earth Sciences*, *203*, 104542.

Xu, F., Hu, B., Zhao, J., Liu, X., Xu, K., Xiong, Z., et al. (2021). Provenance and weathering of sediments in the deep basin of the northern South China Sea during the last 38 kyr. *Marine Geology*, *440*, 106602.

Xue, H. J., Chai, F., Pettigrew, N., Xu, D. Y., Shi, M., Xu, J. P. (2004). Kuroshio intrusion and the circulation in the South China Sea. Journal of Geophysical

Research-Oceans, *109*(C2), C02017.

Yang, X., Peng, X., Qiang, X., Niu, L., Zhou, Q., & Wang, Y. (2016). Chemical weathering intensity and terrigenous flux in South China during the last 90,000 Years—Evidence from magnetic signals in marine sediments. *Frontiers in Earth Science*, *4*, 47.

Yang, Y., Xiang, R., Zhang, L., Zhong, F., & Zhang, M. (2020). Is the upward release of intermediate ocean heat content a possible engine for low-latitude processes? *Geology*, *48*, 579–583.

Yuan, Y., Tseng, Y. H., Yang, C., Liao, G., Chow, C. H., Liu, Z., et al. (2014). Variation in the Kuroshio intrusion: Modeling and interpretation of observations collected around the Luzon Strait from July 2009 to March 2011. *Journal of Geophysical Research: Oceans*, *119*, 3447–3463.

Zhang, C., Yang, S., Huang, X., Dou, Y., Li, F., Xu, X., et al. (2022). Sea level change and Kuroshio intrusion dominated Taiwan sediment source-to-sink processes in the northeastern South China Sea over the past 244 kyrs. *Quaternary Science Reviews*, *287*, 107558.

Zhao, S., Liu, Z., Colin, C., Zhao, Y., Wang, X., & Jian, Z. (2018). Responses of the East Asian Summer Monsoon in the low−latitude South China Sea to high−latitude millennial-scale climatic changes during the last glaciation: Evidence from a high-resolution clay mineralogical record. *Paleoceanography and Paleoclimatology*, *33*, 745–765.

Zhao, W., Zhou, C., Tian, J., Yang, Q., Wang, B., Xie, L., et al. (2014). Deep water circulation in the Luzon Strait. *Journal of Geophysical Research: Oceans*, *119*, 790–804.

Zheng, X., Kao, S., Chen, Z., Menviel, L., Chen, H., Du, Y., et al. (2016). Deepwater circulation variation in the South China Sea since the Last Glacial Maximum. *Geophysical Research Letters*, *43*, 8590–8599.

Zheng, X., Li, A., Wan, S., Jiang, F., Kao, S., Johnson, C. (2014). ITCZ and ENSO pacing on East Asian winter monsoon variation during the Holocene: Sedimentological evidence from the Okinawa Trough. *Journal of Geophysical Research: Oceans*, *119*, 4410–4429.

Zhong, Y., Chen, Z., Li, L., Liu, J. G., Li, G., Zheng, X. F., Wang, S. H., et al. (2017). Bottom water hydrodynamic provinces and transport patterns of the northern South China Sea: Evidence from grain size of the terrigenous sediments. *Continental Shelf Research*, *140*, 11–26.

Zhong, Y., Wilson, D. J., Liu, J., Wan, S., Bao, R., Liu, J., et al. (2021). Contrasting sensitivity of weathering proxies to Quaternary climate and sea-level fluctuations on the southern slope of the South China Sea. *Geophysical Research Letters*, *48*, e2021GL096433.

Zhong, Y. (2022). Response of heterogeneous depositional regime in the northern South China Sea to climate change since the Last Glacial Maximum. [Dataset]. Zenodo. https://doi.org/10.5281/zenodo.7238364.

Zhu, Y. H., Sun, J. C., Wang, Y. G., Li, S. J., Xu, T. F., Wei, Z. X., et al. (2019). Overview of the multi-layer circulation in the South China Sea. *Progress in Oceanography*, *175*, 171-182.

Zong, Y. (2004). Mid-Holocene sea-level highstand along the Southeast Coast of China. *Quaternary International*, *117*(1), 55–67.

Figure Captions

Figure 1. Location of sediment cores and modern geographic, atmospheric, and oceanographic features. The studied sites F07 and S11 are indicated by red stars and other sites referred to in the text or figures are marked by white dots. (a) Map of regional atmospheric and ocean circulation. Modern locations of the Intertropical Convergence Zone (ITCZ) in July and January are indicated by the light-pink lines, while the summer and winter westerlies are shown by the dark blue arrows. Also shown schematically are the East Asian summer monsoon (red arrows), East Asian winter monsoon (grey arrows), Kuroshio Current (magenta arrow), and North Equatorial Current (thick red arrow). Inset panel shows a meridional bathymetric profile through the South China Sea (along the yellow dashed line in panel a), with colours indicating dissolved oxygen content (in ml/l). Figure was generated using Ocean Data View (Schlitzer, 2002) based on data from the World Ocean Atlas (Garcia et al., 2014). NPIW, North Pacific Intermediate Water; PDW, Pacific Deep Water; SCSDW, South China Sea Deep Water; SCSIW, South China Sea Intermediate Water. (b) Details of ocean current systems and clay and magnetic mineral inputs to the northern SCS. White lines and labels indicate major river systems and minor branches. The Pearl River contains three branches (the Xi, Bei and Dong Rivers). The area east of the Pearl River is denoted EPR (as in text). Small coloured arrows indicate ocean currents (Z. Liu et al., 2016). Large coloured arrows represent fluvial sediment input fluxes (units: Mt/a, from Milliman & Meade, 1983), coloured according to their dominant clay mineralogy. Coloured circles illustrate the distribution of S-ratios in river sediments, indicating magnetite versus hematite

content (Kissel et al., 2016, 2017). The inflow of Pacific Deep Water (PDW) is also shown schematically with a red arrow.

Figure 2. End-member modelling results for Core F07 grain-size data. (a) Coefficients of determination (R^2) for models with 1 to 10 end-members. (b) Angular deviations (in degrees) between the reconstructed and observed data sets for models with 1 to 10 end-members. (c) Three modelled end-members (EM1-3) for the terrigenous fraction in Core F07. (d) Variations of mean grain size, median grain size, sand/silt/clay content, and end-member abundances of EM1-3 from 0 to 24 ka in Core F07. Grey bars indicate cold intervals, including the Younger Dryas (YD), Heinrich Stadial 1 (HS1), and the Last Glacial Maximum (LGM). Yellow bar indicates the warm interval of the Bølling/Allerød (B/A), while the Holocene Optimum (HO) is also labelled.

Figure 3. Ternary diagram for major clay groups (illite + chlorite, kaolinite, and smectite) in cores F07 and S11 and comparison to regional sources. The dotted lines indicate mixing lines between the three major riverine end-members. Data for the Pearl River from Liu et al. (2007), data from Taiwan rivers from Liu et al. (2008), data from Luzon rivers from Liu et al. (2009), and data from East of Pearl River (EPR) from Liu et al., (2019). Data from ODP Site 1144 from Hu et al. (2012), data from Core MD12-3434 from Zhao et al. (2018), data from Core CS11 from Shen et al. (2022), and data from sites in the deep basin of the northeastern SCS from Z. Liu et al. (2016). The orange arrow indicates a shift away from Pearl River (or EPR) sources in Core F07

during the deglaciation that may be attributed to sea-level rise.

Figure 4. Temporal variations in clay mineralogy, magnetic properties, and grain size in relation to sea level and ocean circulation reconstructions. (a) Relative sea level (RSL) curves. Pink and blue lines represent global (Lambeck et al., 2014) and western Pacific (East China Sea) RSL (Liu et al., 2004), respectively. Pink, green, and blue symbols represent RSL for the Southeast China Coast (Zong, 2004), Sunda Shelf (Hanebuth et al., 2000), and Red Sea (Grant et al., 2014), respectively. (b) Kaolinite/illite ratio from cores F07 (this study), S11 (this study), GeoB16602-4 (J. Liu et al., 2017), and MD12-3434 (Zhao et al., 2018). (c) S-ratio from cores F07 (this study), S11 (this study), PC338 (M. Li et al., 2018a), and B9 (Zhong et al., 2021). The dashed horizontal lines are the average values for each geographic group (Kissel et al., 2020). (d) End-member EM2 (coarse silt component) and χ_{ARM}/SIRM from Core F07 (this study). (e) χ_{ARM}/SIRM from Core S11 (this study). (f) χ_{ARM}/χ from Core 10E203 from the northeastern SCS (NESCS) (Zheng et al., 2016). (g) $^{231}Pa/^{230}Th$ in Bermuda Rise Core GGC05, as a qualitative indicator for the strength of the Atlantic meridional overturning circulation (AMOC) (McManus et al., 2004). (h) Nd isotopic composition of fossil fish debris (FD) ($\varepsilon_{Nd\text{-}FD}$) from Core MD01-2420 in the northwestern Pacific Ocean, as an indicator of North Pacific Intermediate Water (NPIW) formation (Horikawa et al., 2021). (i) Record of $\delta^{18}O$ values from the NGRIP Greenland ice core (North Greenland Ice Core Project members, 2004). Warm intervals are the Holocene Optimum (HO; yellow shading) and the Bølling/Allerød (B/A; orange). Cold intervals are the Younger Dryas (YD) and

Heinrich Stadial 1 (HS1) (blue-grey), and the Last Glacial Maximum (LGM; grey).

Figure 5. Temporal variations in clay mineralogy and grain size in relation to EASM and Kuroshio Current reconstructions. (a) Stalagmite $\delta^{18}O$ records from Sanbao Cave (red curve) (Cheng et al., 2016) and June 21 insolation at 30°N (orange curve; Laskar et al., 2004). (b) End-member EM2 at Site PC338 (M. Li et al., 2018b) and end-member EM1 in Core F07 (this study) from the northern SCS. (c-e) Smectite/(illite + chlorite) ratios from Core F07 (this study), site MD05-2904 (Liu et al., 2010), and Core S11 (this study). (f) Proxies for the Kuroshio Current intrusion into the SCS, indicated by the smectite/(illite + chlorite) ratio from Core CS11 (Shen et al., 2022) and the warm-water diatom species (%) from ODP Site 1144 in the northern SCS (Jiang et al., 2006). (g) East Asian winter monsoon (EAWM) strength indicated by the stacked normalized mean grain size (MGS) from Chinese loess sections (Kang et al., 2020), and Intertropical Convergence Zone (ITCZ) latitudinal variations indicated by ln(Ti/Ca) ratios in Core MD05-2920 (Tachikawa et al., 2011). Warm intervals are the Holocene Optimum (HO; yellow shading) and the Bølling/Allerød (B/A; orange). Cold intervals are the Younger Dryas (YD) and Heinrich Stadial 1 (HS1) (blue-grey), and the Last Glacial Maximum (LGM; grey).

Figure 6. Schematic representation of terrigenous sediment input and transport during (a) the glacial sea-level lowstand, (b) deglacial cold periods influenced by sea-level rise, (c) deglacial warm periods influenced by sea-level rise, and (d) the mid-late Holocene.

Left panels show map view and right panels show cross-section view across the basin. Abbreviations: EPR, East of Pearl River; KC, Kuroshio Current; KI, Kuroshio Intrusion; LGM, Last Glacial Maximum; NPIW, North Pacific Intermediate Water; PDW, Pacific Deep Water. Symbols '+' and '-' indicate strengthening or weakening, respectively, of particular inputs or currents. See text for further discussion.

Figure 1.

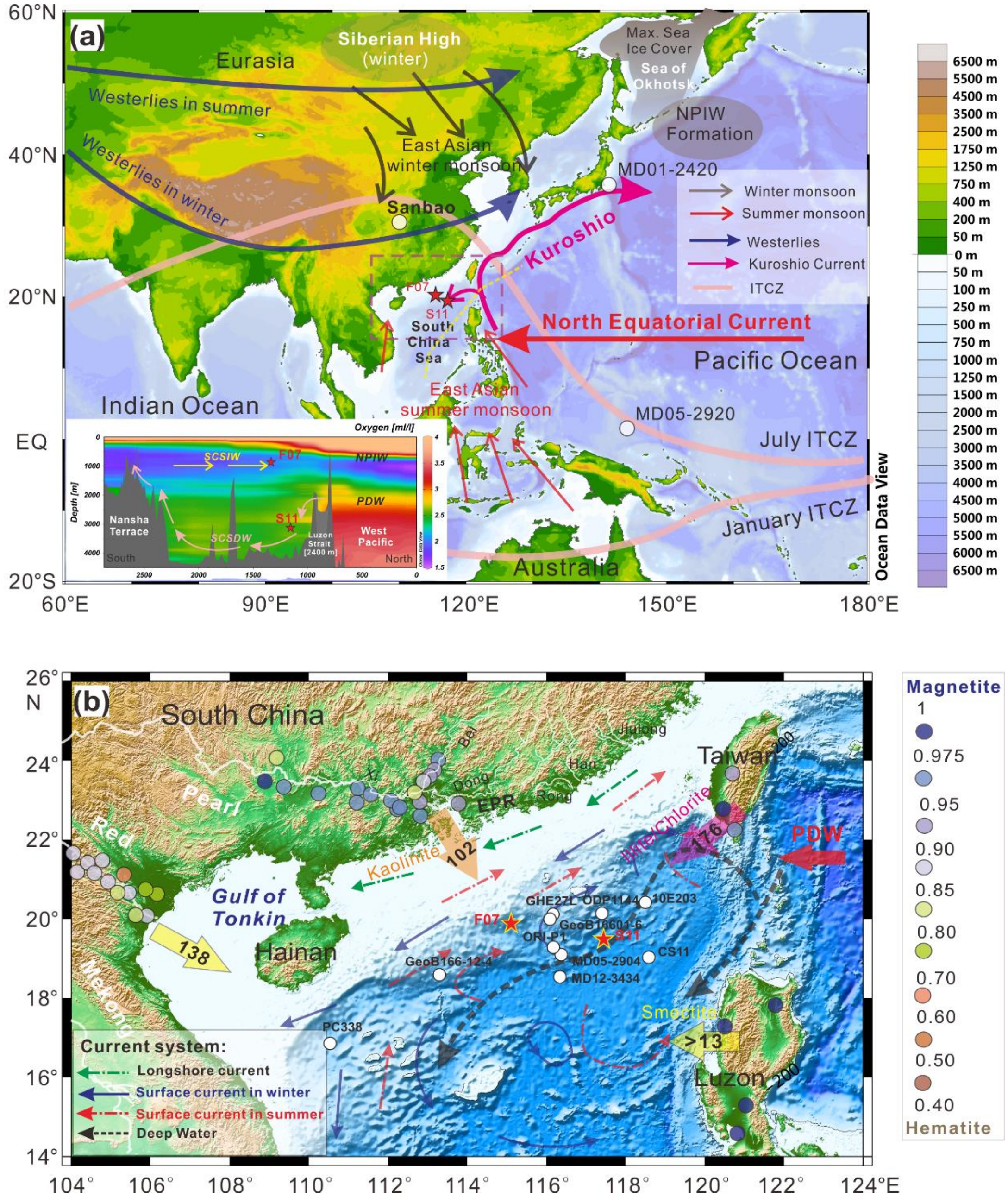
(a)
60°N
40°N
20°N
EQ
20°S
60°E
90°E
120°E
150°E
180°E
Eurasia
Siberian High
(winter)
Max. Sea
Ice Cover
Sea of
Okhotsk
NPIW
Formation
Westerlies in summer
Westerlies in winter
East Asian
winter monsoon
Sanbao
MD01-2420
Kuroshio
F07
S11
South
China
Sea
North Equatorial Current
Pacific Ocean
Indian Ocean
East Asian
summer monsoon
MD05-2920
July ITCZ
January ITCZ
Australia
Winter monsoon
Summer monsoon
Westerlies
Kuroshio Current
ITCZ
Oxygen [ml/l]
Depth [m]
SCSIW
NPIW
PDW
SCSDW
Nansha
Terrace
Luzon
Strait
[2400 m]
West
Pacific
South
North
Ocean Data View
6500 m
5500 m
4500 m
3500 m
2500 m
1750 m
1250 m
750 m
400 m
200 m
50 m
0 m
50 m
100 m
250 m
500 m
750 m
1000 m
1250 m
1500 m
2000 m
2500 m
3000 m
3500 m
4000 m
4500 m
5000 m
5500 m
6000 m
6500 m
(b)
26°N
24°
22°
20°
18°
16°
14°
104°
106°
108°
110°
112°
114°
116°
118°
120°
122°
124°E
South China
Pearl
Red
Mekong
Bei
Dong
EPR
Han
Rong
Jiulong
Taiwan
Kaolinite
102
Illite Chlorite
176
PDW
Gulf of
Tonkin
138
Hainan
GHE27L
ODP1144
10E203
F07
GeoB16601-6
S11
ORI-P1
CS11
MD05-2904
GeoB166-12-4
MD12-3434
PC338
Smectite
>13
Luzon
Current system:
Longshore current
Surface current in winter
Surface current in summer
Deep Water
Magnetite
1
0.975
0.95
0.90
0.85
0.80
0.70
0.60
0.50
0.40
Hematite

Figure 2.

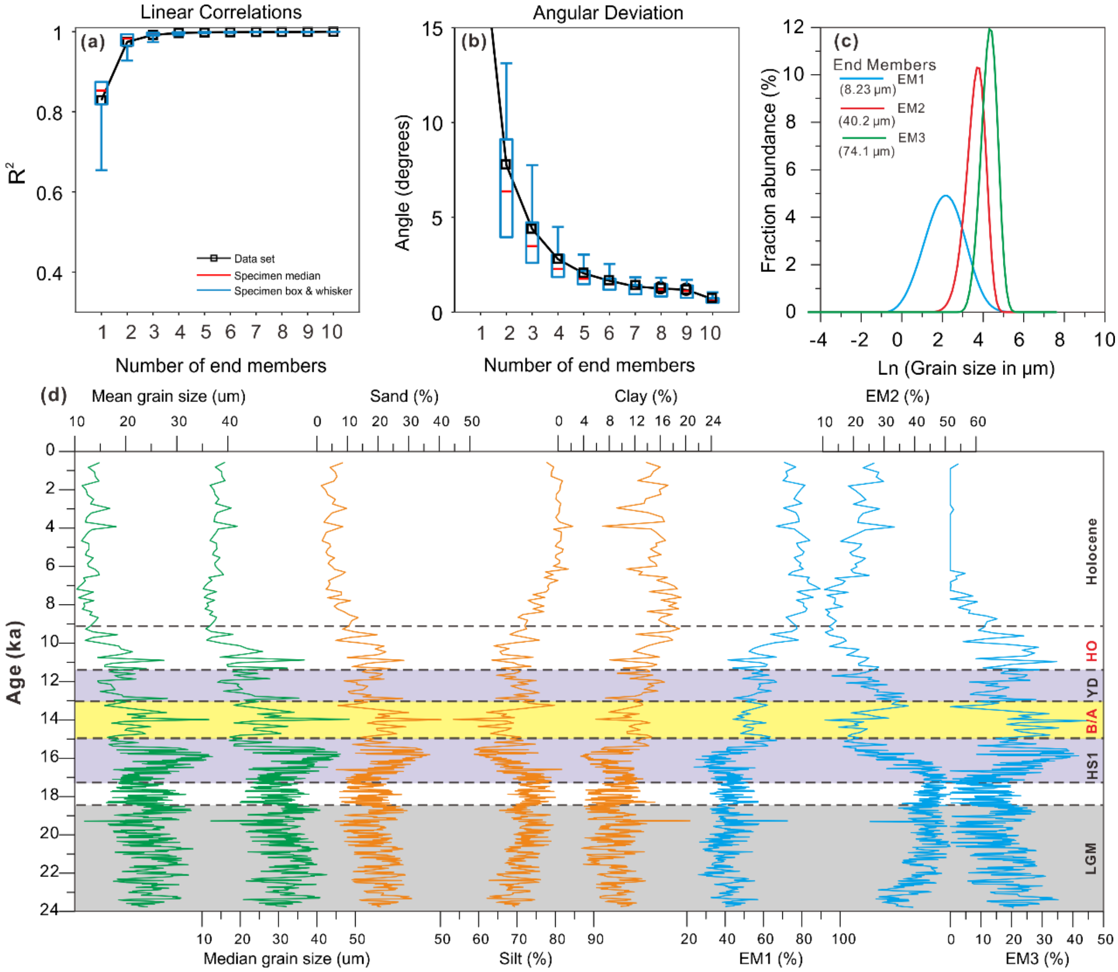

Linear Correlations
Angular Deviation
(a)
(b)
(c)
R²
Angle (degrees)
Fraction abundance (%)
Data set
Specimen median
Specimen box & whisker
Number of end members
Number of end members
End Members
EM1 (8.23 μm)
EM2 (40.2 μm)
EM3 (74.1 μm)
Ln (Grain size in μm)
(d)
Mean grain size (um)
Sand (%)
Clay (%)
EM2 (%)
Age (ka)
Holocene
HO
YD
B/A
HS1
LGM
Median grain size (um)
Silt (%)
EM1 (%)
EM3 (%)

Figure 3.

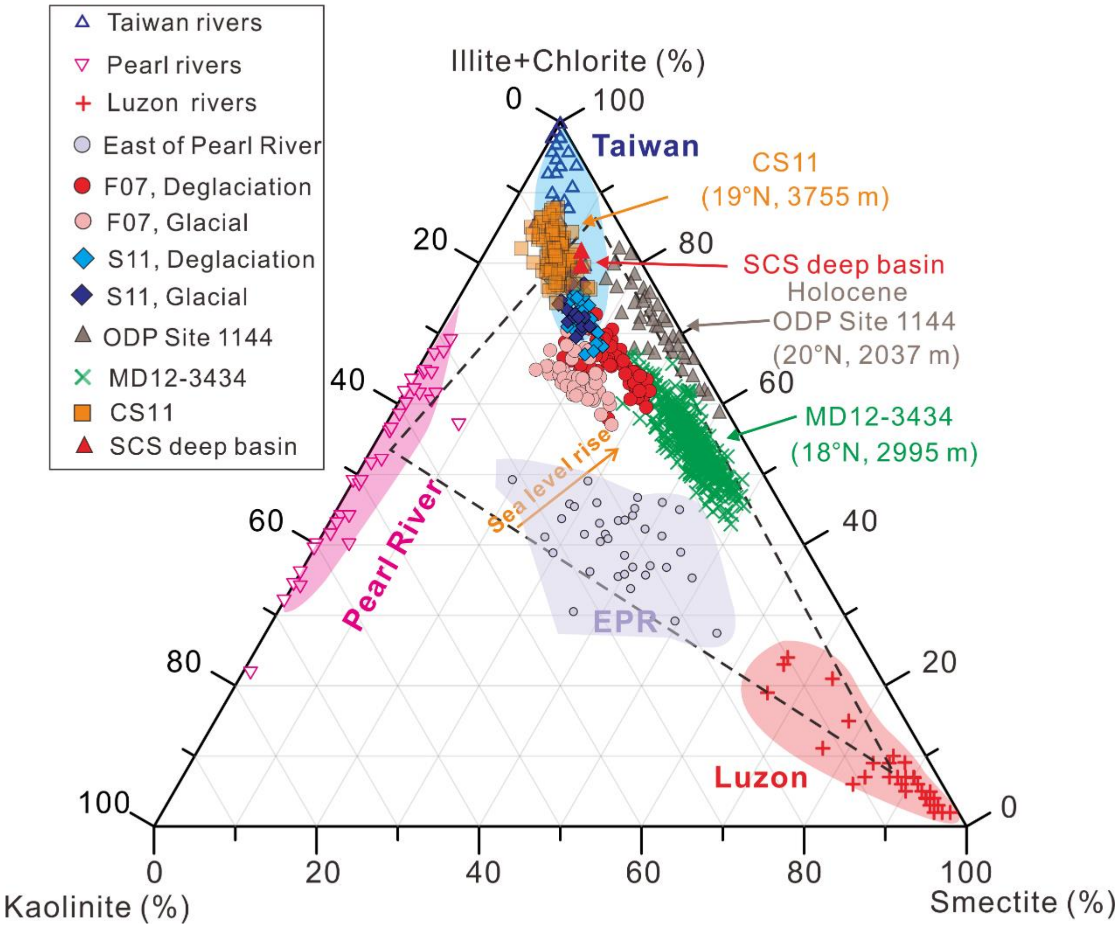

Taiwan rivers
Pearl rivers
Luzon rivers
East of Pearl River
F07, Deglaciation
F07, Glacial
S11, Deglaciation
S11, Glacial
ODP Site 1144
MD12-3434
CS11
SCS deep basin
Illite+Chlorite (%)
Taiwan
CS11
(19°N, 3755 m)
SCS deep basin
Holocene
ODP Site 1144
(20°N, 2037 m)
MD12-3434
(18°N, 2995 m)
Sea level rise
Pearl River
EPR
Luzon
Kaolinite (%)
Smectite (%)
0
20
40
60
80
100

Figure 4.

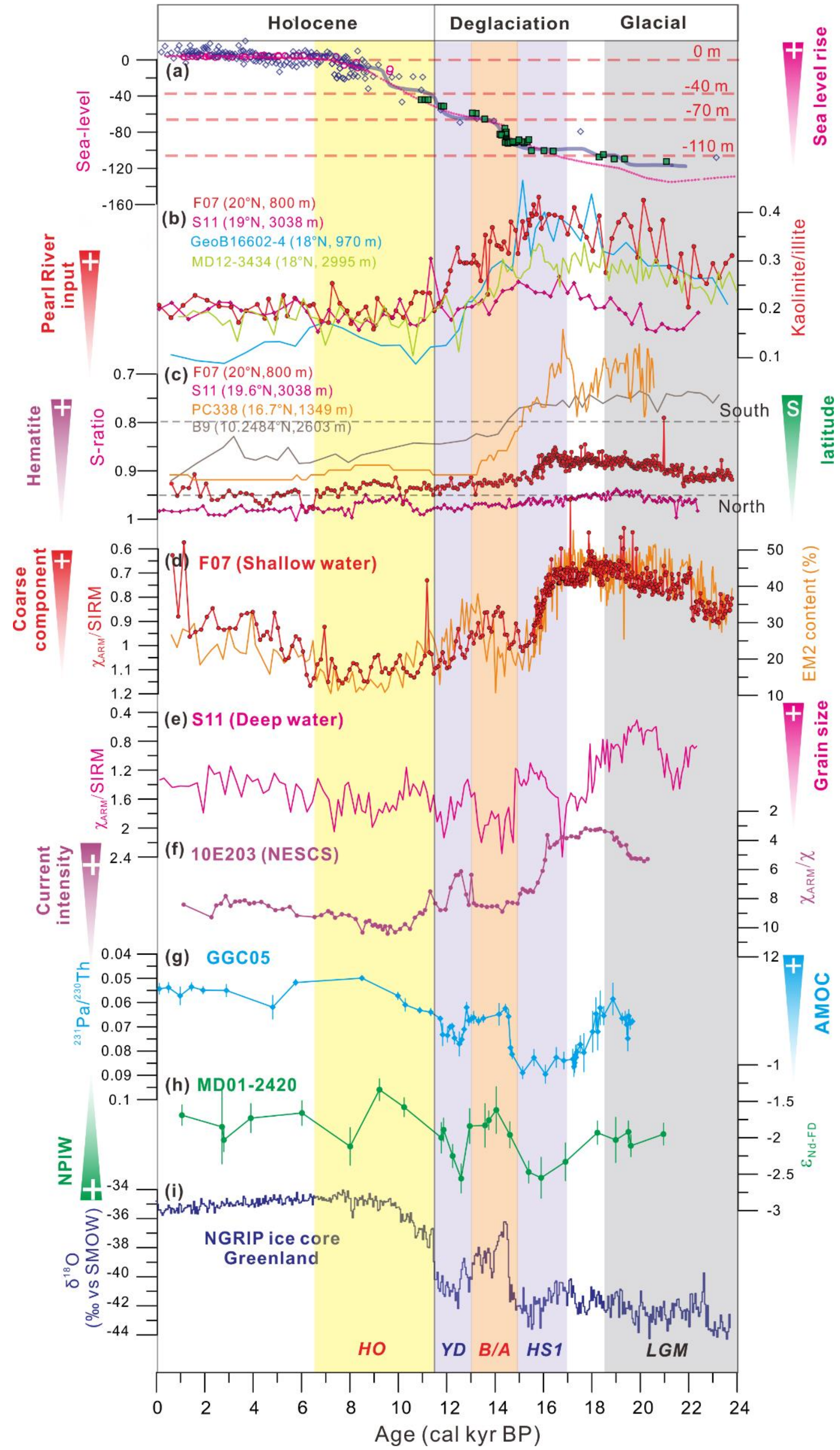

Holocene
Deglaciation
Glacial
(a)
0 m
-40 m
-70 m
-110 m
Sea-level
Sea level rise
(b)
F07 (20°N, 800 m)
S11 (19°N, 3038 m)
GeoB16602-4 (18°N, 970 m)
MD12-3434 (18°N, 2995 m)
Pearl River input
Kaolinite/illite
(c)
F07 (20°N,800 m)
S11 (19.6°N,3038 m)
PC338 (16.7°N,1349 m)
B9 (10.2484°N,2603 m)
South
North
Hematite
S-ratio
latitude
(d) F07 (Shallow water)
Coarse component
EM2 content (%)
(e) S11 (Deep water)
Grain size
(f) 10E203 (NESCS)
Current intensity
(g) GGC05
AMOC
(h) MD01-2420
NPIW
(i)
NGRIP ice core Greenland
HO
YD
B/A
HS1
LGM
Age (cal kyr BP)

Figure 5.

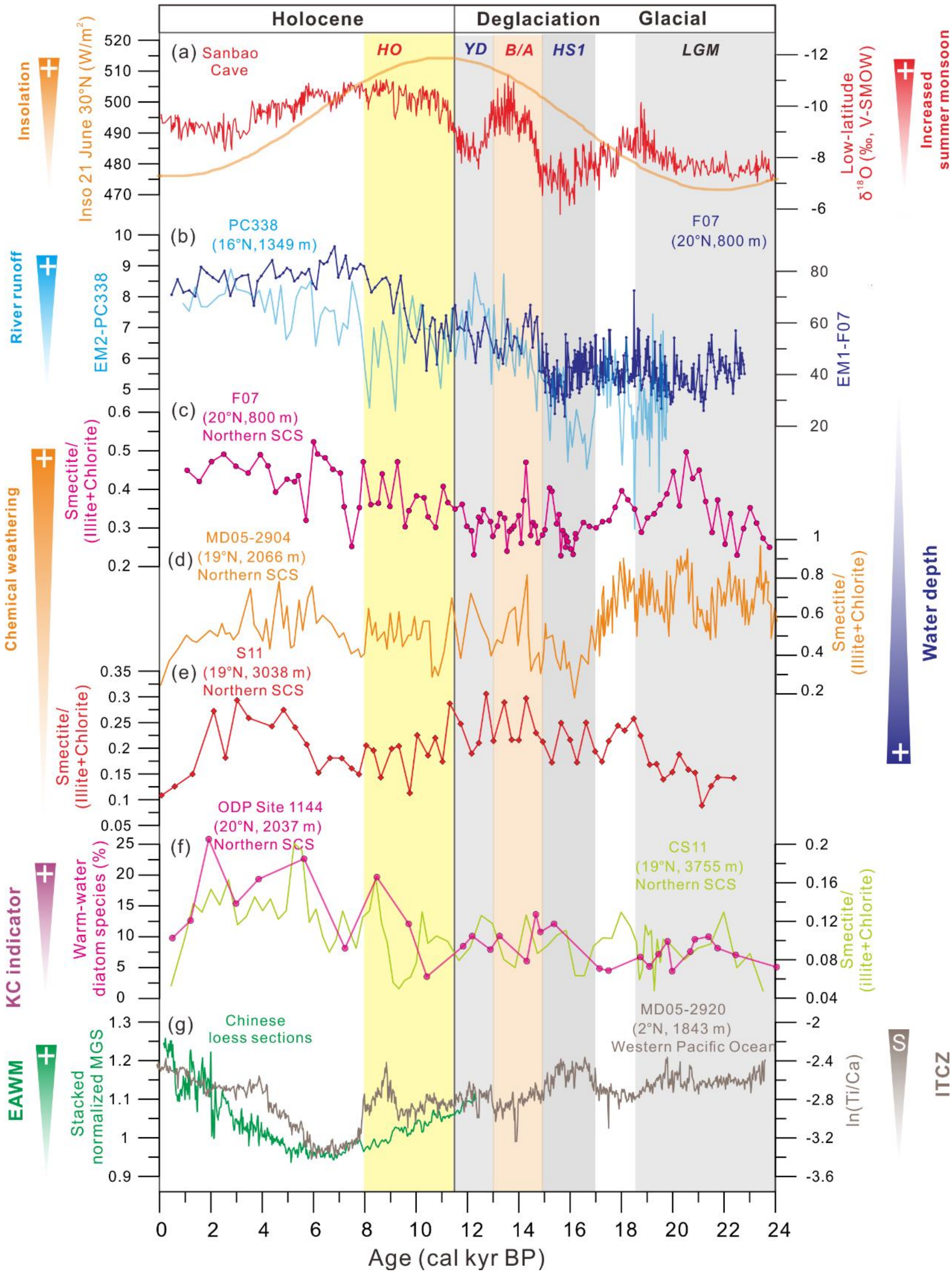

Holocene
Deglaciation
Glacial
HO
YD
B/A
HS1
LGM
(a) Sanbao Cave
Insolation
Inso 21 June 30°N (W/m²)
Low-latitude δ¹⁸O (‰, V-SMOW)
Increased summer monsoon
(b) PC338 (16°N,1349 m)
F07 (20°N,800 m)
River runoff
EM2-PC338
EM1-F07
(c) F07 (20°N,800 m) Northern SCS
Smectite/ (Illite+Chlorite)
Chemical weathering
(d) MD05-2904 (19°N, 2066 m) Northern SCS
Smectite/ (Illite+Chlorite)
Water depth
(e) S11 (19°N, 3038 m) Northern SCS
Smectite/ (Illite+Chlorite)
(f) ODP Site 1144 (20°N, 2037 m) Northern SCS
CS11 (19°N, 3755 m) Northern SCS
KC indicator
Warm-water diatom species (%)
Smectite/ (illite+Chlorite)
(g) Chinese loess sections
MD05-2920 (2°N, 1843 m) Western Pacific Ocean
EAWM
Stacked normalized MGS
ln(Ti/Ca)
ITCZ
S
Age (cal kyr BP)

Figure 6.

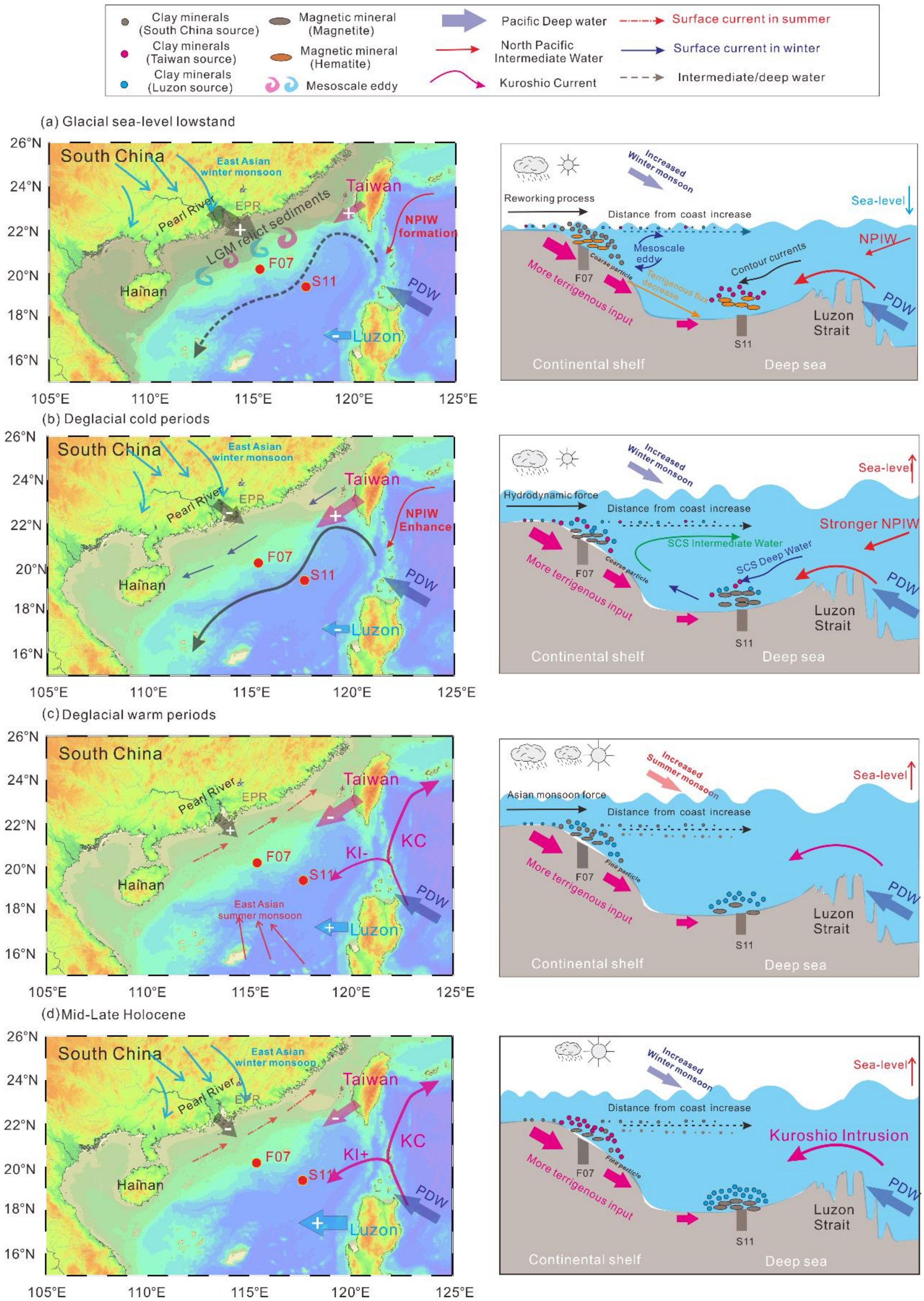

Clay minerals (South China source)
Clay minerals (Taiwan source)
Clay minerals (Luzon source)
Magnetic mineral (Magnetite)
Magnetic mineral (Hematite)
Mesoscale eddy
Pacific Deep water
North Pacific Intermediate Water
Kuroshio Current
Surface current in summer
Surface current in winter
Intermediate/deep water
(a) Glacial sea-level lowstand
(b) Deglacial cold periods
(c) Deglacial warm periods
(d) Mid-Late Holocene
South China
East Asian winter monsoon
Pearl River
EPR
Taiwan
LGM relict sediments
NPIW formation
NPIW Enhance
F07
S11
Hainan
PDW
Luzon
KC
East Asian summer monsoon
Increased Winter monsoon
Increased Summer monsoon
Reworking process
Hydrodynamic force
Asian monsoon force
Distance from coast increase
Sea-level
Mesoscale eddy
Contour currents
Stronger NPIW
SCS Intermediate Water
SCS Deep Water
Kuroshio Intrusion
More terrigenous input
Luzon Strait
Continental shelf
Deep sea

Supporting Information for

Interactions between depositional regime and climate proxies in the northern South China Sea since the Last Glacial Maximum

Xuesong Wang [1,8], Yi Zhong [2*], Peter D. Clift [3], Yingci Feng [4], David J. Wilson [5], Stefanie Kaboth-Bahr [6], André Bahr [7], Xun Gong [1,8], Debo Zhao [9], Zhong Chen [4], Yanan Zhang [2], Yuhang Tian [4], Yuxing Liu [2], Xiaoyu Liu [2], Jiabo Liu [11], Wenyue Xia [2], Huihui Yang [2,10], Wei Cao [2], Qingsong Liu [2,12*]

[1]Institute for Advanced Marine Research, China University of Geosciences, Guangzhou, China

[2]Centre for Marine Magnetism (CM[2]), Department of Ocean Science and Engineering, Southern University of Science and Technology, Shenzhen 518055, PR China

[3]Department of Geology and Geophysics, Louisiana State University, Baton Rough, LA, 70803, USA

[4]Key Laboratory of Ocean and Marginal Sea Geology, South China Sea Institute of Oceanology, Innovation Academy of South China Sea Ecology and Environmental Engineering, Chinese Academy of Sciences, Guangzhou 511458, China

[5]Department of Earth Sciences, University College London, London, UK

[6]Institute of Geosciences, University of Potsdam, Potsdam-Golm, Germany

[7]Institute of Earth Sciences, Heidelberg University, Im Neuenheimer Feld 234-236, 69120, Heidelberg, Germany

[8]State Key laboratory of Biogeology and Environmental Geology, Hubei Key Laboratory of Marine Geological Resources, University of Geosciences, Wuhan 430074, China

[9]Key Laboratory of Marine Geology and Environment, Institute of Oceanology, Chinese Academy of Science, Qingdao

[10]Scholl of Environment, Harbin Institute of Technology, Harbin, China

[11]Paleomagnetism and Planetary Magnetism Laboratory, School of Geophysics and Geomatics, China University of Geosciences, Wuhan, Hubei 430074, China

[12]Shanghai Sheshan National Geophysical Observatory, Shanghai, 201602, China

*Corresponding author: Yi Zhong (zhongy@sustech.edu.cn), Qingsong Liu (qsliu@sustech.edu.cn)

Introduction

The supporting information contains Text S1, Table S1 and S2. Text S1 covers the regional setting, including details of fluvial sediment discharges. Table S1 denotes the calibrated ages of cores F07 and S11 and Table S2 denotes Magnetic properties of surface sediments from the studied cores and potential source regions.

Text S1. Regional setting

The South China Sea (SCS) is the largest semi-enclosed marginal sea in the low-latitude Pacific Ocean, and both its sedimentary inputs and surface currents are strongly influenced by the East Asian monsoon system (Figure 1a; Wang et al., 2014). This system is controlled by the thermal contrast between the Asian landmass and the tropical Pacific Ocean and it is responsible for high annual precipitation totals, leading to large river discharges into the SCS via several river systems (Liu et al., 2016; Milliman & Meade, 1983). Among them, the three largest rivers from the Asian continent are the Pearl, Red, and Mekong rivers, which supply very high fluxes of terrigenous material to the SCS (~600 Mt/yr) (Figure 1b) (Liu et al., 2011, 2014). Additionally, mountainous rivers in southwestern Taiwan (e.g. Cho-Shui and Kao-Ping rivers) also discharge large amounts of suspended sediments, in total 176 Mt yr^{-1} into the northeastern SCS (Figure 1b) (Dadson et al., 2003). These terrigenous sediment loads are then partially redistributed across the SCS by surface ocean currents (Zhong et al., 2017), specifically the seasonally-reversing clockwise/anticlockwise surface currents driven by the East Asian summer/winter monsoon (Shaw and Chao, 1994), as well as the Guangdong coastal currents (Qu et al., 2006) (Figure 1b).

The surface current systems of the SCS are also strongly modulated by the intrusion of the Kuroshio Current (Xue et al., 2004; Zhu et al., 2019) (Figure 1). This current intrudes into the SCS through the Luzon Strait and is regarded as a key conveyor of tropical climate signals from the open Pacific Ocean to this marginal sea (Chen et al., 2020). The Kuroshio Current intrusion also significantly affects the heat, nutrient, and salinity exchange between the open Pacific Ocean and the SCS, which in turn strongly influences hydrologic processes and hence sediment redistribution in the marginal seas (Wu, 2013).

In contrast to the multiple controls on surface ocean hydrography, the deep water regime of the SCS is predominantly constrained by the inflow and pathway of North Pacific Deep Water (NPDW) into the SCS (Tian et al., 2006) (Figure 1). The NPDW enters the SCS through the Luzon Strait in the deep layer (>1500 m), which is regarded as deep water in the SCS (Figure 1). The SCS deep water upwells into the intermediate water between 350 and 1350 m, and is then exported out of the SCS into the western Pacific Ocean through the Luzon Strait (Qu et al., 2006) at water depths of 500-1500 m, below the shallower inflowing waters of the Kuroshio Current.

Table S1. Raw conventional ^{14}C ages and calibrated ages for cores F07 and S11 and associated sedimentation rates.

Site	Depth (cm)	Material	^{14}C AMS ages ±1σ error (yr BP)	Calibrated ages (yr BP)	Calibrated age range (yr BP)	LSR (cm/ka)
F07-1	16.5	Mixed planktonic foraminifera	4110 ± 30	3920	3681 - 4152	4.21
F07-1	64.5	Mixed planktonic foraminifera	10160 ± 30	11044	10768 - 11236	6.74
F07-1	113.5	Mixed planktonic foraminifera	13640 ± 40	15555	15266 - 15841	10.9
F07-1	263.5	Mixed planktonic foraminifera	15850 ± 50	18292	18042 - 18595	54.8
F07-1	326.5	Mixed planktonic foraminifera	17300 ± 60	19940	19602 - 20243	38.2
F07-1	356.5	Mixed planktonic foraminifera	17910 ± 60	20654	20370 - 20927	42.0
F07-1	433.5	Mixed planktonic foraminifera	20300 ± 70	23431	23106 - 23726	27.7
16ZBS11	10	Mixed planktonic foraminifera	2290 ± 30	1726	1567 - 1877	5.8
16ZBS11	60	Mixed planktonic foraminifera	7080 ± 30	7385	7247 - 7518	8.8
16ZBS11	162	Mixed planktonic foraminifera	12920 ± 40	14603	14299 - 14882	14.1
16ZBS11	280	Mixed planktonic foraminifera	17170 ± 50	19825	19554 - 20089	22.6

AMS, accelerator mass spectrometry

LSR, linear sedimentation rate

Table S2. Magnetic properties of surface sediments from the studied cores and potential source regions.

Region	Sample number		χ_{lf} (10^{-8} m^3/kg)	χ_{ARM} (10^{-8} m^3/kg)	SIRM (10^{-3} Am^2/kg)	S-ratio	Reference
F07	441	Mean $\pm\sigma$	12.26 $\pm$1.61	116.8 $\pm$24.0	1.45 $\pm$0.156	0.90 $\pm$0.02	This study
S11	149	Mean $\pm\sigma$	37.16 $\pm$9.18	248.9 $\pm$105.4	1.78 $\pm$0.62	0.97 $\pm$0.01	This study
Pearl River	18	Mean $\pm\sigma$	48.3 $\pm$34.0	159.7 $\pm$86.8	7.01 $\pm$5.92	0.922 $\pm$0.068	Kissel et al., 2016
Red River	21	Mean $\pm\sigma$	50.3 $\pm$27.7	153.8 $\pm$65.4	19.5 $\pm$12.6	0.87 $\pm$0.099	Kissel et al., 2016
Mekong River	17	Mean $\pm\sigma$	23.3 $\pm$8.7	117 $\pm$48	2.76 $\pm$1.00	0.791 $\pm$0.080	Kissel et al., 2016
Malay Peninsula	4	Mean $\pm\sigma$	4.5 $\pm$2.2	17 $\pm$3	0.27 $\pm$0.10	0.737 $\pm$0.203	Kissel et al., 2017
Sumatra	5	Mean $\pm\sigma$	51.0 $\pm$43.4	183 $\pm$118	5.05 $\pm$4.24	0.962 $\pm$0.015	Kissel et al., 2017
Borneo	5	Mean $\pm\sigma$	2.8 $\pm$1.5	52 $\pm$74	0.31 $\pm$0.14	0.869 $\pm$0.086	Kissel et al., 2017
Luzon Rivers	5	Mean $\pm\sigma$	254.3 $\pm$145.7	611 $\pm$341	25.23 $\pm$145.7	0.983 $\pm$0.019	Kissel et al., 2017
Taiwan	3	Mean $\pm\sigma$	6.7$\pm$0.3	17$\pm$4	0.50 $\pm$0.24	0.963 $\pm$0.021	Kissel et al., 2017

References

Chen, Y. C., Zhai, F. G., & Li, P. L. (2020). Decadal Variation of the Kuroshio Intrusion Into the South China Sea During 1992-2016. *Journal of Geophysical Research-Oceans*, *125*(1), e2019JC015699.

Dadson, S. J., Hovius, N., Chen, H., Dade, W. B., Hsieh, M. L., Willett, S. D., et al. (2003). Links between erosion, runoff variability and seismicity in the Taiwan orogen. *Nature*, *426*, 648-651.

Liu, J. G., Xiang, R., Chen, M. H., Chen, Z., Yan, W., & Liu, F. (2011). Influence of the Kuroshio current intrusion on depositional environment in the northern South China Sea: evidence from surface sediment records. *Marine Geology*, *285*, 59-68.

Liu, Y. L., Gao, S., Wang, Y. P., Yang, Y., Long, J. P., Zhang, Y. Z., et al. (2014). Distal mud deposits associated with the Pearl River over the northwestern continental shelf of the South China Sea. *Marine Geology*, *347*, 43-57.

Liu, Z., Zhao, Y., Colin, C., Stattegger, K., Wiesner, M. G., Huh, C. A., et al. (2016). Source-to-Sink transport processes of fluvial sediments in the South China Sea. *Earth-Science Reviews*, *153*, 238-273.

Milliman, J. D., & Meade, R. H. (1983). World wide delivery of river sediment to the oceans. *Journal of Geology*, *91*(1), 1-21.

Qu, T. D., Du, Y., & Sasaki, H. (2006). South China Sea throughflow: A heat and freshwater conveyor. *Geophysical Research Letters*, *332*(23), 430-452.

Shaw, P. T., & Chao, S. Y. (1994). Surface circulation in the South China Sea. *Deep Sea Research Part I: Oceanographic Research Papers*, *41*(11), 1663-1683.

Tian, J. W., Yang, Q. X., Liang, X. F., Xie, L. L., Hu, D. X., Wang, F., et al. (2006). Observation of Luzon Strait transport. *Geophysical Research Letters*, *33*(19), L19607.

Wang, P., Li, Q., & Tian, J. (2014). Pleistocene paleoceanography of the South China Sea: Progress over the past 20 years. *Marine Geology*, *352*, 381-396.

Wu, C. R., 2013. Interannual modulation of the pacific decadal oscillation (PDO) on the low-latitude western North Pacific. *Progress in Oceanography*, *110*, 49-58.

Xue, H. J., Chai, F., Pettigrew, N., Xu, D. Y., Shi, M., Xu, J. P. (2004). Kuroshio intrusion and the circulation in the South China Sea. Journal of Geophysical Research-Oceans, *109*(C2), C02017.

Zhong, Y., Chen, Z., Li, L., Liu, J. G., Li, G., et al. (2017). Bottom water hydrodynamic provinces and transport patterns of the northern South China Sea: Evidence from grain size of the terrigenous sediments. *Continental Shelf Research*, *140*, 11-26.

Zhu, Y. H., Sun, J. C., Wang, Y. G., Li, S. J., Xu, T. F., Wei, Z. X., et al. (2019). Overview of the multi-layer circulation in the South China Sea. *Progress in Oceanography*, *175*, 171-182.